Draft version August 27, 2014
Preprint typeset using LaTeX style emulateapj v. 5/2/11

arXiv:1408.5900v1 [astro-ph.GA] 25 Aug 2014

HST-COS OBSERVATIONS OF AGN. II. EXTENDED SURVEY OF ULTRAVIOLET COMPOSITE SPECTRA FROM 159 ACTIVE GALACTIC NUCLEI

Matthew L. Stevans[1], J. Michael Shull[2], Charles W. Danforth, and Evan M. Tilton
CASA, Department of Astrophysical & Planetary Sciences,
University of Colorado, Boulder, CO 80309, USA

Draft version August 27, 2014

ABSTRACT

The ionizing fluxes from quasars and other active galactic nuclei (AGN) are critical for interpreting their emission-line spectra and for photoionizing and heating the intergalactic medium (IGM). Using far-ultraviolet spectra from the Cosmic Origins Spectrograph (COS) on the *Hubble Space Telescope* (*HST*), we directly measure the rest-frame ionizing continua and emission lines for 159 AGN at redshifts $0.001 < z_{\rm AGN} < 1.476$ and construct a composite spectrum from 475–1875 Å. We identify the underlying AGN continuum and strong EUV emission lines from ions of oxygen, neon, and nitrogen after masking out absorption lines from the H I Lyα forest, 7 Lyman-limit systems ($N_{\rm HI} \geq 10^{17.2}$ cm^{-2}) and 214 partial Lyman-limit systems ($15.0 < \log N_{\rm HI} < 17.2$). The 159 AGN exhibit a wide range of FUV/EUV spectral shapes, $F_\nu \propto \nu^{\alpha_\nu}$ typically with $-2 \leq \alpha_\nu \leq 0$ and no discernible continuum edges at 912 Å (H I) or 504 Å (He I). The composite rest-frame continuum shows a gradual break at $\lambda_{\rm br} \approx 1000$ Å, with mean spectral index $\alpha_\nu = -0.83 \pm 0.09$ in the FUV (1200–2000 Å) steepening to $\alpha_\nu = -1.41 \pm 0.15$ in the EUV (500–1000 Å). We discuss the implications of the UV flux turnovers and lack of continuum edges for the structure of accretion disks, AGN mass inflow rates, and luminosities relative to Eddington values.

Subject headings: galaxies: active — line: profiles — quasars: emission lines – ultraviolet: galaxies

1. INTRODUCTION

The far ultraviolet (FUV) and extreme ultraviolet (EUV) continua of active galactic nuclei (AGN) are thought to form in the black hole accretion disk (Krolik 1999; Koratkar & Blaes 1999), but their ionizing photons can influence physical conditions in the broad emission-line region of the AGN as well as the surrounding interstellar and intergalactic gas. The metagalactic background from galaxies and AGN is also an important parameter in cosmological simulations, as a dominant source of ionizing radiation, critical for interpreting broad emission-line spectra of AGN, intergalactic metal-line absorbers, and fluctuations in the ratio of the Lyα absorbers of H I and He II.

Since the deployment of the first space-borne ultraviolet (UV) spectrographs, astronomers have combined spectral observations of AGN into composite spectra. These composites constrain the intensity and shape of the AGN component of the ionizing photon background. The most direct probe of the FUV and EUV continua in the AGN rest frame comes from observations taken by instruments such as the *International Ultraviolet Explorer* (IUE) and a series of UV spectrographs aboard the *Hubble Space Telescope* (*HST*): the Goddard High Resolution Spectrograph (GHRS), the Faint Object Spectrograph (FOS), the Space Telescope Imaging Spectrograph (STIS), and the Cosmic Origins Spectrograph (COS). Ultraviolet spectra were also obtained by the *Far Ultraviolet Spectroscopic Explorer* (*FUSE*). For AGN at modest redshifts, all of these instruments provide access to the rest-frame Lyman continuum (LyC, $\lambda < 912$ Å), and at $z < 1.5$ they avoid strong contamination from the Lyα-forest absorbers in the spectra of high-redshift AGN. Thus, obtaining access to high-S/N, moderate-resolution UV spectra is crucial for finding a reliable underlying continuum.

This is our second paper, following a AGN composite spectrum presented in Paper I (Shull et al. 2012) based on initial results from COS spectra of 22 AGN at redshifts $0 < z < 1.4$. We analyzed their rest-frame FUV and EUV spectra, taken with the G130M and G160M gratings, whose resolving power $R = \lambda/\Delta\lambda \approx 18,000$ (17 km s^{-1} velocity resolution) allows us to distinguish line blanketing from narrow interstellar and intergalactic absorption lines. Here, in Paper II, we enlarge our composite spectrum from 22 to 159 AGN, confirm the validity of our early results, and explore possible variations of the EUV spectral index with AGN type and luminosity. Both studies were enabled by high-quality, moderate-resolution spectra taken with the Cosmic Origins Spectrograph installed on *HST* during the May 2009 servicing mission. The COS instrument (Green et al. 2012) was designed explicitly for point-source spectroscopy of faint targets, particularly quasars and other AGN used as background sources for absorption-line studies of the intergalactic medium (IGM), circumgalactic medium (CGM), and interstellar medium (ISM). Our survey is based on high-quality spectra of the numerous AGN used in these projects.

Our expanded survey of 159 AGN finds a composite

stevans@astro.as.utexas.edu,michael.shull@colorado.edu
[1] Now at Astronomy Department, University of Texas, Austin, TX, 78712
[2] Also at Institute of Astronomy, Cambridge University, Cambridge CB3 OHA, UK

spectral energy distribution (SED) with frequency index $\alpha_\nu = -1.41 \pm 0.15$ in the rest-frame EUV. This confirms the results of Paper I, where we found $\alpha_\nu = -1.41 \pm 0.21$. We adopt the convention in which rest-frame flux distributions are fitted to power laws in wavelength, $F_\lambda \propto \lambda^{\alpha_\lambda}$, and converted to $F_\nu \propto \nu^{\alpha_\nu}$ in frequency with $\alpha_\nu = -(2 + \alpha_\lambda)$. We caution that these spectral indices are *local* measures of the slope over a small range in wavelength, $\Delta\lambda/\lambda \approx 0.45$. Because of curvature of the AGN spectral distributions, local slopes can be misleading, when compared to different wavelength bands and to objects at different redshift. We return to this issue in Section 3.3 where we discuss possible correlations of indices α_λ with AGN type, redshift, and luminosity and compare indices measured by both *HST*/COS and *FUSE*.

The COS composite spectrum is somewhat harder than that in earlier *HST*/FOS and STIS observations (Telfer et al. 2002) who fitted the continuum (500–1200 Å) with $\alpha_\nu = -1.76 \pm 0.12$ for 184 QSOs at $z > 0.33$. Their sample of 39 radio-quiet AGN had $\alpha_\nu = -1.57 \pm 0.17$. Our fit differs considerably from the *FUSE* survey of 85 AGN at $z \leq 0.67$ (Scott et al. 2004) who found a harder composite spectrum with $\alpha_\nu = -0.56^{+0.38}_{-0.28}$. The different indices could arise in part from the small numbers of targets observed in the rest-frame EUV. Even in the current sample, only 10 or fewer AGN observations cover the spectral range 450 Å $\lesssim \lambda \lesssim$ 600 Å. Another important difference in methodology is our placement of the EUV continuum relative to strong emission lines such as Ne VIII (770, 780 Å), Ne V (570 Å), O II (834 Å), O III (833, 702 Å), O IV (788, 554 Å), O V (630 Å), and O VI (1032, 1038 Å). Identifying and fitting these emission lines requires high S/N spectra. A complete list of lines appears in Table 4 of Paper I. We also use the higher spectral resolution of the COS (G130M and G160M) gratings to distinguish the line-blanketing by narrow absorption lines from the Lyα forest. Increasingly important at higher redshifts, we need to identify and correct for absorption from Lyman-limit systems (LLS) with $N_{HI} \gtrsim 10^{17.2}$ cm^{-2} and partial Lyman-limit systems (pLLS) with $N_{HI} = 10^{15} - 10^{17.2}$ cm^{-2}. The historical boundary at $10^{17.2}$ cm^{-2} occurs where the photoelectric optical depth $\tau_{HI} = 1$ at the 912 Å Lyman edge.

In Paper I, our 22 AGN ranged in redshift from $z = 0.026$ to $z = 1.44$, but included only four targets at sufficient redshift to probe the rest-frame continuum below 550 Å. Our new survey contains 159 AGN out to $z = 1.476$ with 16 targets at $z > 0.90$, sufficient to probe below 600 Å by observing with G130M down to 1135 Å. In all AGN spectra, we identify the prominent broad emission lines and line-free portions of the spectrum and fit the underlying continua, excluding interstellar and intergalactic absorption lines. In Section 2 we describe the COS data reduction and our new techniques for restoring the continua with a fitting method that corrects for the effects of absorption from the IGM and ISM. In Section 3 we describe our results on the FUV and EUV spectral indices in both individual and composite spectra. Section 4 presents our conclusions and their implications.

2. OBSERVATIONS OF ULTRAVIOLET SPECTRA OF AGN

2.1. *Sample Description*

Table 1 lists the relevant COS observational parameters of our 159 AGN targets, which include AGN type and redshift (z_{AGN}), from NED[3], continuum index (α_λ), fitted rest-frame flux normalization at 1100 Å, observed flux F_λ at 1300 Å, and S/N ratios. We also provide power-law fits to their *HST*/COS spectra (see Section 2.2) and their monochromatic luminosities, λL_λ, at 1100 Å, given by

$$\lambda L_\lambda = (1.32{\times}10^{43}\,\mathrm{erg\ s^{-1}}) \left[\frac{d_L}{100\ \mathrm{Mpc}}\right]^2 \left[\frac{F_\lambda}{10^{-14}}\right] \left[\frac{\lambda}{1100\ \text{Å}}\right] . \quad (1)$$

We converted flux, F_λ (in erg cm^{-2} s^{-1} Å^{-1}) to monochromatic luminosity, $L_\lambda = 4\pi d_L^2 F_\lambda$, using the luminosity distance, $d_L(z)$, computed for a flat ΛCDM universe with $H_0 = 70$ km s^{-1} Mpc^{-1} and density parameters $\Omega_m = 0.275$ and $\Omega_\Lambda = 0.725$ (Komatsu et al. 2011).

The redshift distribution of the sample is shown in Figure 1, and the target distribution in accessible rest-frame wavelength in Figure 2. Our sample consists only of those AGN observed with both the G130M (1135–1460 Å) and G160M (1390–1795 Å) COS gratings, providing the broad wavelength coverage at 17 km s^{-1} resolution needed for our study of the continuum, emission lines, and absorption line blanketing. The COS instrument and data acquisition are described by Osterman et al. (2011) and Green et al. (2012). We retrieved all COS AGN spectra publicly available as of 2013 April 25, but excluded spectra with low signal-to-noise per pixel (S/N < 1) and all BL Lac objects, which are over-represented in the COS archives. We also excluded three targets with abnormal spectra that would complicate the analysis: SDSSJ004222.29-103743.8, which exhibits broad absorption lines; SDSSJ135726.27+043541.4, which features a pLLS longward of the COS waveband; and UGCA 166, which Gil de Paz & Madore (2005) classify as a blue compact dwarf galaxy. This leaves 159 AGN for analysis.

2.2. *Data Acquisition and Processing*

We follow the same procedure as in Paper I for obtaining, reducing, and processing the data. Below, we briefly summarize the procedure and explicitly note improvements or deviations from earlier methods. Many of these techniques of coaddition and continuum fitting were also discussed in our IGM survey (Danforth et al. 2014). Of particular interest in this paper are new techniques for identifying LLS and pLLS absorbers, measuring their H I column densities, and using that information to correct the continuum. Our analysis proceeds through the following steps:

[3] NASA/IPAC Extragalactic Database (NED) is operated by the Jet Propulsion Laboratory, California Institute of Technology, under contract with the National Aeronautics and Space Administration, `http://nedwww.ipac.caltech.edu`.

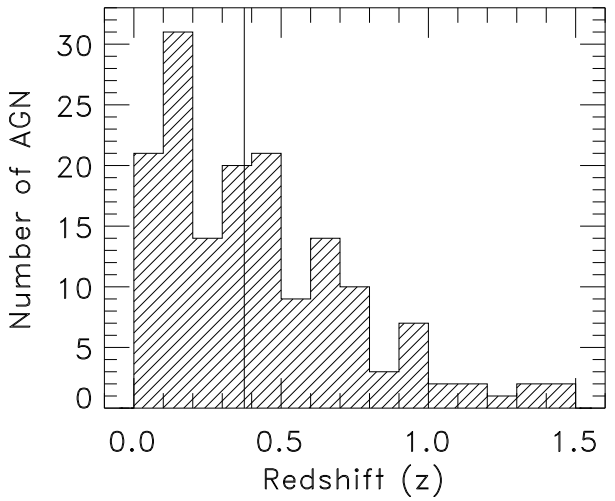

FIG. 1.— Histogram of the redshifts of the 159 AGN in our COS sample. Vertical line marks the median redshift, $\langle z \rangle \approx 0.37$ of the sample.

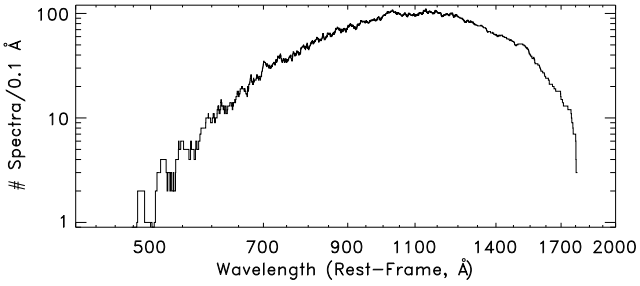

FIG. 2.— Number of AGN targets that contribute to the composite spectrum (see Figure 5) as a function of AGN rest-frame wavelength. Note the rapid decline in targets that probe short wavelengths, with ten or fewer AGN probing $\lambda \leq 600$ Å.

1. **Retrieve exposures.** The CALCOS calibrated exposures were downloaded from the Mikulski Archive for Space Telescopes (MAST) and then aligned and co-added using IDL procedures developed by the COS GTO team[4]. Typical wavelength shifts were a resolution element (∼0.1 Å) or less, and the co-added flux in each pixel was calculated as the exposure-weighed mean of the flux in aligned exposures.

2. **Fit spline functions to spectra.** The raw data contain narrow absorption features that should be excluded from the AGN composite spectrum. Identifying and masking each of these features by hand in all of our spectra would be extremely tedious. For this reason, we utilize a semi-automated routine that removes narrow absorption features and fits the remaining data with a piecewise-continuous function composed of spline functions and Legendre polynomial functions. This spline-fitting process involves first splitting the spectra into 5-10 Å segments and calculating the average S/N per pixel (flux/error) in each segment. Pixels with S/N less than 1.5 σ below their segment S/N are rejected from the fitting process to exclude absorption features and regions of increased noise. This process is repeated iteratively until there is little change between iterations. The median flux values in the segments are then fitted with a spline function. We manually inspect the fits and adjust the identification of rejected regions as necessary. Smoothly varying data are well described by this spline-only method. Near broad emission and other cusp-like features, short segments of piecewise-continuous Legendre polynomials are preferred. More details on the process are given in our IGM survey paper (Danforth et al. 2014).

3. **Deredden spectra.** We correct the fine-grained data and their corresponding spline fits for Galactic reddening, using the empirical mean extinction curve of Fitzpatrick (1999) with a ratio of total-to-selective extinction $R_V = A_V/E(B-V) = 3.1$ and color excesses $E(B-V)$ from NED. In this paper we use values of $E(B-V)$ based on dust mapping by Schlegel et al. (1998) with a 14% recalibration by Schlafly & Finkbeiner (2011). We do not correct for reddening intrinsic to the AGN, although we do not think this could be a substantial effect. We can probably rule out a large amount of dust (see discussion in Section 3.2).

4. **Identify pLLS and LLS absorption.** In Paper I, we identified pLLS absorption by inspecting the spectra for flux decrements or Lyman breaks. For this paper we employ a custom computer script that scans each spectrum for correlated down-pixels at the locations of higher-order Lyman lines of pLLS and LLS absorbers. First, the script divides the spectra by their respective spline fits, normalizing the flux unaffected by IGM absorption to unity. We determine the median flux for 15 pixels that have the same relative spacing as the first 15 H I Lyman lines of a pLLS with a redshift equal to the source AGN. If there is a pLLS, the median will be much less than unity. We then step one pixel to the left, recalculate the relative spacing of the first 15 Lyman lines at this redshift and the median flux for this group of 15 pixels. We repeat this process until we reach the end of the spectrum or a pLLS redshift of zero. The script returns a list of redshifts of system candidates to be inspected. When a system is confirmed, we measure the equivalent widths of up to the first 12 Lyman lines and fit them to a curve of growth (CoG) to determine the column density and Doppler parameter of the system. In Paper I, we found a total of 17 LLS and pLLS systems in 8 of the 22 sight lines, and we were sensitive to systems with column density $\log N_{\rm HI} \geq 15.5$. In this paper, using our new identification method, we confirm the 17 previously identified systems plus 13 unidentified systems above the sensitivity limit $\log N_{\rm HI} \sim 15.5$ in the same 22 sight lines from Paper I. Figure 3 shows examples of pLLS identification and continuum restoration. The lowest column density measurement derived from CoG fitting in this paper is $\log N_{\rm HI} \sim 13.4$.

[4] IDL routines available at
`http://casa.colorado.edu/~danforth/science/cos/costools`

We detect 221 systems (7 LLS and 214 pLLS) in 71 of the 159 AGN sight lines, with absorber redshifts $0.24332 \leq z_a \leq 0.91449$. These absorbers are listed in Table 2 together with our measurements of their redshifts, H I column densities, and Doppler parameters. Of the 221 systems, 167 have column densities $\log N_{\rm HI} \geq 15.0$ whose distribution in column density is shown in Figure 4. We only correct for these 167 systems in our analysis. Systems with $\log N_{\rm HI} = 15.5$ and $\log N_{\rm HI} = 15.0$ have opacity that depress the flux immediately blueward of the Lyman limit by less than 2% and 0.7% respectively. Owing to the multiple correlated Lyman lines used in this identification technique, our sensitivity is better than the local S/N over most of the spectral coverage. Correcting for the opacity of weaker systems ($\log N_{\rm HI} < 15.0$) would have a negligible effect on our analysis of AGN continuum, changing the EUV slope of our composite spectrum by only 0.006.

5. **Restore flux depressed by pLLS and mask unrecoverable flux.** We account for Lyman continuum absorption by measuring the equivalent widths of the first 12 Lyman lines and fitting them with a CoG to estimate the H I column density and Doppler parameter. We use these measurements to correct for the ν^{-3} opacity shortward of each Lyman edge. We correct only the flux below the Lyman limit. When a spectrum has pLLS absorption with column density $\log N_{\rm HI} = 15.0 - 15.9$, we mask the flux between the Lyman limit (911.753 Å) and Lyman-9 (916.429 Å) or ∼4.7 Å redward in the pLLS rest-frame. For a pLLS with $\log N_{\rm HI} \geq 15.9$, we mask from the Lyman limit to Lyman-13 (920.963 Å) or ∼9.2 Å redward. When data blueward of the Lyman limit of LLS or pLLS had $S/N < 1$ or did not appear continuous with two or more regions of continuum redward of the Lyman limit, we masked the data. We also mask regions of the spectra affected by broad absorption from damped Lyα systems and H_2 Lyman bands after qualitative visual inspection. The amount of masking varies for individual cases. Some spectra have one or two gaps of ≤10 Å in the data from observations that were not planned with contiguous wavelength coverage over the entire COS-FUV spectral range. These gaps are masked prior to our continuum analysis.

6. **Shift to rest-frame.** We shift each spectrum to the rest-frame of the AGN by dividing the wavelength array by $(1 + z_{AGN})$.

7. **Mask non-AGN features.** In every spectrum we exclude Galactic Lyα absorption (1215.67 Å) by masking 14 Å on both sides of the line center in the observed frame. We exclude geocoronal emission lines of N I λ1200 and O I λ1304 by masking 2 Å on both sides of N I and 5 Å on both sides of O I. In five spectra we masked the absorption due to the Lyα line of damped Lyα systems.

8. **Resample the spectra.** As in Paper I and Telfer et al. (2002), we resample the spectra to uniform 0.1 Å bins. After resampling, each flux pixel corresponds to a new wavelength bin and is equal to the mean of the flux in the old pixels that overlap the new bin, weighted by the extent of overlap. The error arrays associated with the resampled spectra are determined using a weighting method similar to the flux rebinning. See Equations (2) and (3) in Telfer et al. (2002) for the rebinning formulae.

3. OVERALL SAMPLE COMPOSITE SPECTRUM

3.1. *Composite Construction*

To construct the overall composite spectrum we start by following the bootstrap method of Telfer et al. (2002) and then adapt the construction technique for our unique dataset. To summarize the bootstrap technique, we start near the central region of the output composite spectrum, between 1050 Å and 1150 Å, and normalize the spectra that include the entire central region to have an average flux value of 1 within the central region, which we refer to as the "central continuum window." We then include spectra in sorted order toward shorter wavelengths. Lastly, we include the spectra in sorted order toward longer wavelengths. When a spectrum does not cover the central continuum window, we normalize it to the partially formed composite by finding the weighted-mean normalization constant within multiple emission-line-free continuum windows, calculated using Equation (4) of Telfer et al. (2002). We form two independent composite spectra simultaneously: one of the fine-grained spectra showing the line-blanketing by the Lyα forest and interstellar absorption lines, and another of the spline fits to the individual spectra. The spline fits pass over the narrow absorption lines.

With our unique dataset and spline fits, we adjust the composite construction method in five ways. First, with the identification in Paper I of broad emission lines from highly ionized species below 800 Å, we were able to restrict the normalization of the spectra at the highest redshifts to two narrow regions of continuum-like windows at 660-670 Å and 715-735 Å. This is in contrast to using all of the flux, including that from emission lines below 800 Å in the calculation of the normalization constant, as was done in our initial method. Our second adjustment also limits the normalization calculation to regions of continuum, which is our primary interest. We refine and narrow the continuum windows above 800 Å to wavelengths 855-880 Å, 1090-1105 Å, 1140-1155 Å, 1280-1290 Å, 1315-1325 Å, and 1440-1465 Å. For our third adjustment we choose the region between 855-880 Å as the central continuum window, because it is the largest of the narrowed EUV continuum windows with a large number of contributing spectra. Fourth, we note that the bootstrapping technique can be sensitive to the ordering in which one includes the spectra, especially at the beginning of the process when only a handful of spectra determine the shape of the composite. Therefore, we increase the number of spectra normalized at only the central continuum window from 40 to 70 by decreasing the required overlap with the central continuum window from 100% to 50%. Lastly, because we are interested in

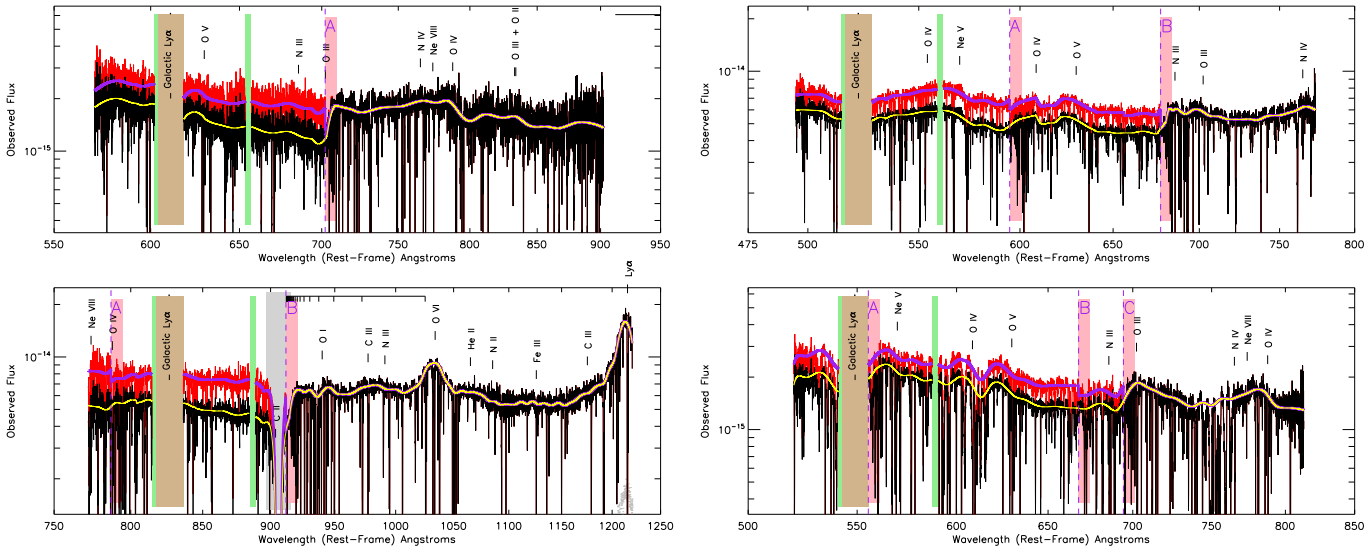

FIG. 3.— Examples of restoring flux depressed by pLLSs: black line shows flux before restoration and red line after restoration; yellow line shows spline fit before restoration and purple line spline after restoration. Vertical colored boxes mark data excluded from composite and slope measurements: light brown boxes exclude Galactic Lyα absorption; light green boxes exclude oxygen airglow emission; pink boxes exclude absorption from LLSs and pLLSs; gray boxes eliminate large features not intrinsic to AGN emission or observational gaps in data. Panels (top left and right, and bottom left and right) show: SDSS J084349.49+411741.6 with absorber A ($z_{\rm LLS} = 0.533$, $\log N_{\rm HI} = 16.77$); PG 1522+101, with two absorbers: system A ($z_{\rm LLS} = 0.518$, $\log N_{\rm HI} = 16.32$) and system B ($z_{\rm LLS} = 0.729$, $\log N_{\rm HI} = 16.60$); SDSS J161916.54+334238.4 with system A ($z_{\rm LLS} = 0.269$, $\log N_{\rm HI} = 16.40$) and system B ($z_{\rm LLS} = 0.471$, $\log N_{\rm HI} = 16.84$); PG 1338+416 with three absorbers: system A ($z_{\rm LLS} = 0.349$, $\log N_{\rm HI} = 16.37$), system B ($z_{\rm LLS} = 0.621$, $\log N_{\rm HI} = 16.30$), and system C ($z_{\rm LLS} = 0.686$, $\log N_{\rm HI} = 16.49$).

characterizing the shape of the underlying continuum as a power law, we follow the approach of Vanden Berk et al. (2001) and combine the spectra as a geometric mean, which preserves power-law slopes. We also provide a median-combined composite, which preserves the relative shape of the emission features.

Below 700 Å, the number of AGN spectra contributing to each 0.1 Å bin in Figure 2 declines steadily. Several AGN listed in Table 1 do not appear in this figure because their short-wavelength spectra are masked out, owing to LLS absorption, airglow, and pLLS edges. The final overall sample composite spectra (both geometric-mean and median) are presented in two panels of Figure 5, covering rest-frame wavelengths from 475-1785 Å. In each panel, we show both the fine-grained data with absorption lines included and the spline-fit continuum composites. In the geometric-mean spectrum, which we regard as the better characterization of the AGN composite, the effects of line-blanketing by the Lyα forest can be seen in the difference between the spline-fit composite and the real data composite. Figure 6 shows the optical depth, τ_λ, arising from line-blanketing of the continuum by the Lyα forest at $\lambda < 1150$ Å. We derive optical depths from the difference in fluxes (red and black) in the geometric mean composite, shown in the top panel of Figure 5.

To characterize the continuum slope of the composite spectrum, we follow the simple approach of Vanden Berk et al. (2001). We calculate the slope between continuum regions of maximum separation on either side of the spectral break, which is clearly present in the composite around 1000 Å. Because the flux distribution, F_λ, flattens at shorter wavelengths, the two power-law fits pass under the observed spectrum and match at the break. To satisfy this condition, we first calculate the slope of

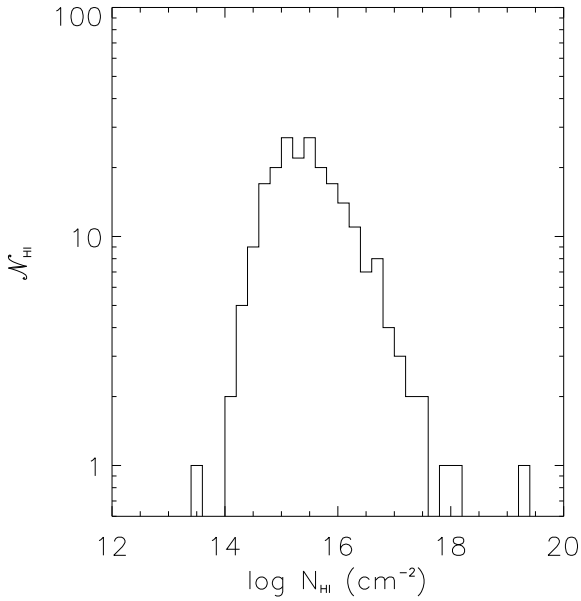

FIG. 4.— Distribution of strong H I absorbers in column density $N_{\rm HI}$, with a range in absorber redshifts ($0.24326 < z_a < 0.91449$) accessible to coverage with the COS moderate-resolution gratings (G130M and G160M). Along 71 AGN sight lines at $z_{\rm AGN} > 0.26$, we identified 214 pLLS with $15.0 \leq \log N_{\rm HI} < 17.2$ and seven LLS with $\log N_{\rm HI} \geq 17.2$.

a line connecting the minima of the two best continuum regions in log-log space. We then divide the entire spectrum by this line, find the wavelengths of the minima, and calculate the slope of the line that connects the second pair of minima. This results in a line that does not cross the composite. We perform this calculation twice,

once in the EUV and again in the FUV. We find a mean EUV spectral index $\alpha_\lambda = -0.59$ between line-free windows centered at 724.5 Å and 859 Å, and mean FUV index $\alpha_\lambda = -1.17$ between 1101 Å and 1449 Å. These wavelength indices correspond to frequency indices α_ν of -1.41 (EUV) and -0.83 (FUV).

3.2. *Uncertainties*

We now discuss sources of random and systematic uncertainty in the composite spectral indices. As in Paper I, we fit two power laws to the spline composite spectrum, with indices $\alpha_{\rm FUV}$ and $\alpha_{\rm EUV}$, and match them at a break wavelength, which we find to be $\lambda_{\rm br} \approx 1000$ Å, consistent with Paper I and accurate to ~ 50 Å. Although this gradual break is apparent in the composite, its presence is less clear in the individual spectra, owing to the limited spectral range of the COS observations and to strong emission lines of O VI λ1035 and Lyβ λ1025 near the break wavelength. Because the sample of AGN in Paper I had no targets between $0.16 < z < 0.45$, most rest-frame spectra lay either blueward or redward of the 1000 Å break. In our new sample, 55 AGN have redshifts in that range, but we do not distinguish a clear break in individual spectra. With the limited wavelength coverage of COS (G130M, G160M), any single AGN spectrum does not have access to the four continuum windows needed to measure two distinct power laws that straddle the break.

To quantify the uncertainty in the fitting of the composite spectrum, we explore the sources of uncertainty described by Scott et al. (2004), including the effects of intrinsic variations in the shape of the SEDs, Galactic extinction, and formal statistical fitting errors. As in Paper I, we do not include the effects of intrinsic absorbers or interstellar lines, as these absorption lines are easily removed with our moderate-resolution COS spectra. However, we do consider the effects from the strongest systems in the Lyα forest. The largest source of uncertainty comes from the natural variations in the slope of the contributing spectra. We estimate this uncertainty by selecting 1000 bootstrap samples with replacement from our sample of 159 AGN spectra. The resulting distributions of spectral index in frequency lead to mean values: $\alpha_{\rm EUV} = -1.41 \pm 0.15$ and $\alpha_{\rm FUV} = -0.83 \pm 0.09$ in the EUV and FUV. Figure 7 shows a montage of spectra for individual AGN, illustrating the wide range of spectral slopes and emission-line strengths.

We also investigated the range of uncertainties arising from UV extinction corrections from two quantities: $E(B-V)$ and R_V. We alter the measured $E(B-V)$ by $\pm 16\%$ ($1\,\sigma$) as reported by Schlegel et al. (1998). We deredden the individual spectra with $E(B-V)$ multiplied by 1.16 or 0.84, compile the spectra into a composite, and fit the continua. Over these ranges, we find that the index $\alpha_{\rm EUV}$ changes by $(+0.064, -0.022)$ while $\alpha_{\rm FUV}$ changes by $(+0.046, -0.023)$. Next, we estimate the sensitivity to deviations from the canonical value $R_V = 3.1$, which Clayton, Cardelli, & Mathis (1988) found to vary from $R_V = 2.5$ to $R_V = 5.5$. We follow Scott et al. (2004) and deredden individual spectra with $R_V = 2.8$ and $R_V = 4.0$ and compiling the spectra into composites. We find that $\alpha_{\rm EUV}$ changes by $(+0.041, -0.051)$ and $\alpha_{\rm FUV}$ by $(+0.032, -0.059)$. We estimate the uncertainties arising from correcting pLLS absorption of strength $\log N_{\rm HI} \geq 15.0$ by altering the measured column densities by $\pm 1\,\sigma$ as reported in Table 2. We find that $\alpha_{\rm EUV}$ changes by $(+0.037, -0.010)$ and $\alpha_{\rm FUV}$ by $(+0.011, -0.011)$. The formal statistical errors for the spectral indices are negligible (< 0.001), owing to the high S/N ratio of our composite spectra. Thus, we do not include them in the final quoted uncertainties. We add the random uncertainties of cosmic variance with the systematic effects of correcting for extinction in quadrature and estimate the total uncertainties to be ± 0.15 for $\alpha_{\rm EUV}$ and ± 0.09 for $\alpha_{\rm FUV}$.

As noted earlier, we do not correct for AGN dust, but small amounts could be present, as long as they do not produce a strong turnover in the far-UV fluxes. We can rule out a large amount of intrinsic extinction, if it obeys a selective extinction law, $A(\lambda)/A_V$, that rises steeply at short (UV) wavelengths. Otherwise, we would see steep curvature in the rest-frame EUV, rather than a power law.

3.3. *Comparison to Other Composite Spectra*

Ultraviolet spectra of AGN have been surveyed by many previous telescopes, including the *International Ultraviolet Explorer* (O'Brien et al. 1988) and the *HST* Faint Object Spectrograph (Zheng et al. 1997). More recent AGN composite spectra were constructed from data taken with *HST*/FOS+STIS (Telfer et al. 2002), *FUSE* (Scott et al. 2004), and *HST*/COS (Shull et al. 2012 and this paper). Figure 8 compares the *HST*/COS composites with previous studies with *HST*/FOS+STIS and *FUSE*. Our current COS survey finds essentially the same EUV spectral index, $\alpha_\nu = -1.41 \pm 0.15$, as found in Paper I, $\alpha_\nu = -1.41 \pm 0.22$, but with better statistics and coverage to shorter wavelengths (below 500 Å). This consistency is reassuring, as our current composite includes 159 AGN spectra, compared with 22 AGN in the initial COS study (Paper I). The *HST*/COS EUV index, $\alpha_\nu \approx -1.4$ is slightly harder than the *HST*/FOS+STIS value, $\alpha_\nu = -1.57 \pm 0.17$, found by Telfer et al. (2002) for 39 radio-quiet AGN. However, both *HST* surveys found indices steeper than the *FUSE* slope, $\alpha_\nu = -0.56^{+0.38}_{-0.28}$ (Scott et al. 2004), a puzzling discrepancy that we now investigate.

The differences between continuum slopes found in *FUSE* and COS composite spectra are likely to arise from four general factors: (1) continuum placement beneath prominent EUV emission lines; (2) line blanketing by the Lyα forest and stronger (pLLS) absorbers; (3) continuum windows that span an intrinsically curved AGN spectrum; and (4) possible correlation of slope and AGN luminosity. High-S/N spectra at the moderate resolution of COS (G130M/G160M) are critical for identifying the underlying continuum near the strong EUV emission lines of O III, O IV, and O V and the Ne VIII doublet ($\lambda\lambda$770, 780). The COS spectral resolution also allows us to fit over the narrow H I absorbers in the Lyα forest (factor 2) and restore the continuum absorbed by the stronger systems (LLS and pLLS). Factor 3 is a more subtle effect, but it may be the most important. The COS wavelength coverage (1135–1795 Å) is broader than that of *FUSE* (912–1189 Å), and it provides line-free continuum windows above and below 1100 Å, spanning an intrinsically curved SED. This allows us to construct a

two-component spectrum with indices $\alpha_\nu = -1.41 \pm 0.15$ in the EUV (500-1000 Å) and $\alpha_\nu = -0.83 \pm 0.09$ in the FUV (1200-2000 Å) with a break at $\lambda_{\rm br} \approx 1000 \pm 25$ Å. Many of the COS sight lines observe higher-redshift AGN that sample different regions of the SED than those of *FUSE*. Shortward of 912 Å, we place the continuum below a number of prominent emission lines, using nearly line-free continuum windows at 665 ± 5 Å, 725 ± 10 Å, and 870 ± 10 Å. Factor 4 refers to possible selection effects of AGN luminosity with redshift. Previous samples used targets at a variety of redshifts and luminosities, observed with different spectral resolution, FUV throughput, and instruments. All of the UV composite spectra (*HST* and *FUSE*) are based on the available UV-bright targets (Type-1 Seyferts and QSOs) studied with *IUE* and the *Galaxy Evolution Explorer* (*GALEX*). Most of these AGN were chosen as background sources for studies of IGM, CGM, and Galactic halo gas. Although these targets are not a complete, flux-limited sample of the AGN luminosity function (e.g., Barger & Cowie 2010), they probably are representative of UV-bright QSOs, at least at redshifts $z < 0.4$.

Figure 9 compares the average AGN redshift per wavelength bin for the COS and *FUSE* surveys, overlaid on the line-free continuum windows. Evidently, the COS targets are at systematically higher redshift, and their wavelength coverage is broader than that of *FUSE*. The average AGN luminosity also differs, longward and shortward of the break. At $\lambda \approx 800$ Å, the COS and *FUSE* composites are both probing similar luminosities. As shown in the top panel of Figure 9, the two spectral slopes are fairly similar between 650–1000 Å, and the only difference comes from the sudden decline in *FUSE* fluxes between 1090–1140 Å. Lacking the longer-wavelength continuum windows, the *FUSE* spectra were unable to fit the break in spectral slope at longer wavelengths. Figure 10 shows the distributions of spectral index α_λ and the effects of the available continuum windows falling longward or shortward of the 1000 Å break. The two-power-law fits possible with COS data allow us to measure the spectral curvature and distinguish between FUV and EUV slopes. This was not done with the *FUSE* composite fits.

In summary, we believe the *HST*/COS composite spectra are superior owing to their higher spectral resolution (G130M and G160M gratings) allowing us to resolve and mask out the Lyα forest and restore the continuum from stronger (LLS and pLLS) absorbers. The higher S/N of the COS spectra allow us to identify and resolve prominent UV/EUV emission lines and fit a more accurate underlying continuum. As shown in Figures 2 and 7, the COS composite still contains fewer than 10 AGN at $z > 1$ that probe the rest-frame continuum at $\lambda < 600$ Å. These numbers are larger than in the earlier surveys, but the small sample means that the composite spectrum remains uncertain at the shortest wavelengths.

3.4. *Trends with Redshift, AGN Type, and Luminosity*

As in Paper I, we explore trends within the *HST*/COS AGN sample by constructing composite spectra based on various parameters and subsamples. Figure 11 shows the distributions of index α_λ in redshift, AGN activity type, Galactic foreground reddening, and monochromatic (1100 Å) luminosity. In each panel, two horizontal lines denote the sample-mean values: $\langle\alpha_\lambda\rangle = -0.59$ for the rest-frame EUV (500-1000 Å) band and $\langle\alpha_\lambda\rangle = -1.17$ for the rest-frame FUV (1200-2000 Å) band. The spectral indices extend over a wide range of AGN luminosities and activity types, with no obvious trend or correlation. Galactic reddening does not appear to produce any difference in the index. There may be subtle trends in the distribution of α_λ with redshift, because we are observing the rest-frame flux from an intrinsically curved spectral energy distribution (SED). At low redshift ($z < 0.25$) there are many AGN with steep slopes, $\alpha_\lambda < -1.5$, indicating hard UV spectra. However, only seven AGN have spectra with $\alpha_\lambda < -1.5$. At higher redshift ($z > 0.5$) there are few AGN with slopes $\alpha_\lambda < -1.5$, and the survey contains few AGN at the most extreme redshifts ($z > 1$). Many more have soft spectra with slopes $\alpha_\lambda > -0.5$.

3.5. *Softened UV Spectra and Continuum Edges*

Accretion disk (AD) model spectra have recently been investigated by a number of groups (Davis et al. 2007; Laor & Davis 2011; Done et al. 2012; Slone & Netzer 2012) with a goal of comparing to UV and EUV spectra. The observed far-UV spectral turnover at $\lambda < 1000$ Å limits the maximal disk temperature to $T_{\rm max} \approx 50,000$ K. Model atmospheres computed with the *TLUSTY* code (Hubeny et al. 2001) and including winds driven from inner regions of the disk predict a spectral break near 1000 Å, arising from the Lyman edge (912 Å) and wind-truncation of the hot inner part of the disk (Laor & Davis 2014). In a standard multi-temperature accretion-disk models with blackbody spectra in annular rings (Pringle 1981) the radial temperature distribution scales as $T(r) \propto (M_{\rm BH}\dot{M}/r^3)^{1/4}$. In their models of wind-ejecting disks, Slone & Netzer (2012) suggest that the spectral shape is governed by the radial profile of $\dot{M}(r)$, and the radius $r_{1/2}$ where half the disk mass has been ejected. Their observational predictions are based on the removal of hot accreting gas from the inner regions of the AD and accompanying removal of energy from the UV-emitting portions of the SED. A large mass accretion rate throughout the AD produces higher luminosities and shifts the SED to shorter (UV) wavelengths. The closer $r_{1/2}$ comes to the innermost stable circular orbit, $r_{\rm ISCO}$, the more FUV and EUV radiation will be emitted.

Slone & Netzer (2012) used the sensitivity of the EUV spectral index, $\alpha_{456-912}$ between 456–912 Å, to constrain accretion properties outside $R_{\rm ISCO}$, the radius of the innermost stable circular orbit around a black hole (see their Figure 7). Their model is governed by mass accretion rates, $\dot{M}_{\rm in}$ and $\dot{M}_{\rm out}$, at the inner and outer disk radii of the disk, relative to the Eddington accretion rate $\dot{M}_{\rm edd}$ and luminosity $L/L_{\rm edd}$ relative to the Eddington luminosity, $L_{\rm edd}$. From the observed EUV spectral index, $\alpha_{456-912} \approx -1.4$, we constrain the mean AGN accretion rate and luminosity to values $\dot{M}_{\rm in}/\dot{M}_{\rm edd} < 0.1$ and $L/L_{\rm edd} < 0.2$. We caution that these inferences are subject to the validity of accretion-disk model atmospheres, including effects of external irradiation, uncertainty in where energy is being deposited, and the role of magnetic field energy dissipation. In addition, disk photospheres

may differ from those of hot stars, with spatially variable $\tau = 1$ surfaces.

Laor & Davis (2014) explore similar disk-truncation models, solving for the radial structure of a disk with mass loss. They find that the wind mass loss rate, $\dot{M}_{\rm wind}$, becomes comparable to the total accretion rate $\dot{M}$ at radii a few tens of gravitational radii, (GM/c^2). Line-driven winds set a cap of $T_{\rm max} < 10^5$ K on their disks, which in most cases are truncated well outside the ISCO radius. These models are consistent with the observed SED turnover at $\lambda < 1000$ Å that is weakly dependent on luminosity L and black-hole mass $M_{\rm BH}$. Their models of line-driven winds also cap AD effective temperatures, $T_{\rm eff} < 10^5$ K. The UV spectral turnover is produced by both an H I Lyman edge and the limit on disk temperature.

Standard models of accretion disk atmospheres are predicted to exhibit H I and He I continuum edges at 912 Å and 504 Å, respectively. This issue and the EUV (soft X-ray) spectra of accretion disks have been discussed by many authors (e.g., Kolykhalov & Sunyaev 1984; Koratkar & Blaes 1999; Done et al. 2012). The absence of any continuum absorption at 912 Å in the composite spectrum was noted in Paper I, where we set an optical depth limit of $\tau_{\rm HI} < 0.03$. From the 159-AGN composite (see Figures 5 and 8) our limit is now $\tau_{\rm HI} < 0.01$ derived from the flux around 914.5 Å and 910.5 Å. The limit for the He I edge at 504 Å is less certain because of the difficulty in fitting the local continuum under neighboring broad EUV emission lines. However, from the general continuum shape between 480-520 Å, we can limit the He I continuum optical depth to $\tau_{\rm HeI} < 0.1$. Additional COS/G140L data now being acquired toward 11 AGN at redshifts $1.5 \leq z \leq 2.2$ probe the rest-frame c ontinua at $\lambda < 400$ Å with good spectral coverage at the 504 Å edge. We continue to see no He I continuum edge.

4. DISCUSSION AND CONCLUSIONS

We now summarize the results and implications of our *HST*/COS survey of AGN spectral distributions in the AGN rest-frame FUV and EUV. Using spectra of 159 AGN taken with *HST*/COS G130M and G160M gratings, we constructed a 2-component composite spectrum n the EUV (500-1000 Å) and FUV (1200-2000 Å). These two spectral fits match at a break wavelength $\lambda_{\rm br} \approx 1000$ Å, below which the SED steepens to $F_\nu \propto \nu^{-1.41}$. The EUV index is the same as found in Paper I, but with smaller error bars. It is slightly harder than the index, $\alpha_\nu = -1.57 \pm 0.17$, found from the HST/FOS+STIS survey (Telfer et al. 2002) for radio-quiet AGN, but much softer than the index, $\alpha_\nu = -0.56^{+0.38}_{-0.28}$, from the *FUSE* survey (Scott et al. 2004). These composite spectra are based on small numbers of AGN with redshifts ($z \geq 1$) sufficient to probe below 600 Å. However, the *HST*/COS survey provides a superior measure of the true underlying continuum. Our G130M/G160M data have sufficient spectral resolution and signal to noise to mask out narrow lines from the Lyα forest and restore the continuum from stronger (LLS and pLLS) absorbers. We also fit the continuum below the prominent broad EUV emission lines using nearly line-free continuum windows at 665 ± 5 Å, 725 ± 10 Å, and 870 ± 10 Å.

Our primary conclusions are as follows:

1. The HST/COS composite spectrum follows a flux distribution with $F_\nu \propto \nu^{-0.83 \pm 0.09}$ for AGN rest-frame wavelengths 1200-2000 Å and $F_\nu \propto \nu^{-1.41 \pm 0.15}$ for 500-1000 Å. This EUV spectral index is slightly harder than that used in recent simulations (Haardt & Madau 2012) of IGM photoionization and photoelectric heating.

2. Individual spectra of the 159 AGN surveyed exhibit a wide range of spectral indices in the EUV, with typical values between $-2 \leq \alpha_\nu \leq 0$. These indices are *local* slopes and not characteristic of the spectral energy distribution over the full UV/EUV band,

3. The composite SED exhibits a turnover at $\lambda < 1000$ Å, characteristic of accretion disk models in which the maximum temperature $T_{\rm max} < 10^5$ K and the inner disk is truncated by line-driven winds.

4. We see no continuum edges of H I (912 Å) or He I (504 Å), with optical depth limits $\tau_{\rm HI} < 0.01$ and $\tau_{\rm HeI} < 0.1$. The absence of these edges suggests that accretion disk atmospheres differ from those of hot stars, because of external irradiation or inverted temperature structures arising from magnetic energy dissipation.

5. We find no obvious correlations of the EUV spectral index with interstellar reddening, AGN type, redshift, or luminosity (λL_λ at 1100 Å). Such trends are difficult to pick out, because the observable *HST*/COS (G130M/G160M) wavelength band (1135-1795 Å) covers different portions of the SED over the AGN redshifts $0.001 < z < 1.476$) in our sample. The quoted indices, α_λ are *local* slopes that fall either in the FUV or EUV depending on AGN redshift.

6. The mean EUV slopes, compared to models of wind-truncated thin accretion disks, constrain the mean accretion rate in the inner disk and the AGN luminosity to values $\dot{M}_{\rm in}/\dot{M}_{\rm edd} < 0.1$ and $L/L_{\rm edd} < 0.2$ relative to their Eddington rates.

The order-of-magnitude improvement in sensitivity offered by COS over previous spectrographs has greatly increased the number of targets available for moderate-resolution UV spectroscopy. Some of these spectra have S/N below the threshold chosen for this survey, and many are low-resolution (G140L) rather than G130M/G160M used here. Nevertheless, some of these archival spectra will provide EUV coverage down to 500 Å (with ∼40 AGN) and to 912 Å (with ∼100 AGN). Additional data at AGN rest wavelengths 400-500 Å would be helpful in fitting the SED deeper into the EUV, where fewer than ten AGN sight lines have been probed to date with COS/G130M. Currently, our composite spectrum includes 10 AGN that contribute at $\lambda \leq 600$ Å but only two AGN at $\lambda < 500$ Å. As noted in Paper I, one can

explore even shorter rest-frame wavelengths (304–500 Å) using the sample of "He II quasars" (Worseck et al. 2011; Syphers et al. 2011; Shull et al. 2010) that probe the He II epoch of reionization at $z \approx 2.5 - 3.5$. In Hubble Cycle 21, we are observing 11 new AGN targets at $z = 1.45$ to $z = 2.13$, using the lower-resolution (G140L) grating. The first ten of these spectra have now been acquired. After reduction, they should improve the accuracy of the composite spectrum down to 400 Å and provide more sight lines that cover the He I 504 Å continuum edge. Our intent is to create a composite AGN spectrum between 350 Å and 1800 Å, using *HST*/COS archival spectra of AGN with a variety of types and luminosities.

We thank the COS/GTO team for help on the calibration and verification of COS data. We acknowledge helpful discussions with Shane Davis, Ari Laor, and Jim Pringle on accretion disk models and thank the referee for helpful comments that encouraged us to explore the differences between COS and *FUSE* composite spectra. This research was supported by NASA grants NNX08-AC14G and NAS5-98043 and the Astrophysical Theory Program (NNX07-AG77G from NASA) at the University of Colorado Boulder. JMS thanks the Institute of Astronomy, Cambridge University, for their stimulating scientific atmosphere and support through the Sackler Visitor Program.

REFERENCES

Barger, A. J., & Cowie, L. L. 2001, ApJ, 718, 1235
Clayton, G. C., Cardelli, J. A., & Mathis, J. S. 1988, ApJ, 329, L33
Danforth, C. W., Tilton, E. M., Shull, J. M., et al. 2014, ApJ, submitted (arXiv:1402.2655)
Davis, S. W., Woo, J.-H., & Blaes, O. M. 2007, ApJ, 668, 682
Davis, S. W., & Laor, A. 2011, ApJ, 728, 98
Done, C., Davis, S. W., Jin, C., Blaes, O., & Ward, M. 2012, MNRAS, 420, 1848
Finn, C. W., Morris, S. M., Crighton, N. H. M., et al. 2014, MNRAS, 440, 3317
Fitzpatrick, E. L. 1999, PASP, 111, 63
Gil de Paz, A., & Madore, B. F. 2005, ApJ, 156, 345
Green, J. C., Froning, C., Osterman, S., et al. 2012, ApJ, 744, 60
Haardt, F., & Madau, P. 2012, ApJ, 746, 125
Hubeny, I., Blaes, O., Krolike, J. H., & Agol, E. 2001, ApJ, 559, 680
Kolykhalov, P. I., & Sunyaev, R. A. 1984, Adv. Space Res. 1984, 3, 249
Komatsu, E., Smith, K. M., Dunkley, J., et al. 2011, ApJS, 192, 18
Koratkar, A., & Blaes, O. 1999, PASP, 111, 1
Krolik, J. H. 1999, Active Galactic Nuclei (Princeton: Princeton Univ. Press)
Laor, A., & Davis, S. W. 2014, MNRAS, 438, 3024
O'Brien, P. T., Wilson, R., & Gondalekhar, P. 1988, MNRAS, 233, 801
Osterman, S., Green, J., Froning, C., et al. 2011, Ap&SS, 335, 257
Pringle, J. E. 1981, ARA&A, 19, 137
Schlafly, E. F., & Finkbeiner, D. P. 2011, ApJ, 737, 103
Schlegel, D. J., Finkbeiner, D. P., & Davis, M. 1998, ApJ, 500, 525
Scott, J. E., Kriss, G. A., Brotherton, M., et al. 2004, ApJ, 615, 135
Shull, J. M., France, K., Danforth, C. W., Smith, B. D., & Tumlinson, J. 2010, ApJ, 722, 1312
Shull, J. M., Stevans, M., & Danforth, C. W. 2012, ApJ, 752, 152
Slone, O., & Netzer, H. 2012, MNRAS, 426, 656
Syphers, D., Anderson, S. F., Zheng, W., et al. 2011, ApJ, 726, 111
Telfer, R., Zheng, W., Kriss, G. A., & Davidsen, A. F. 2002, ApJ, 656, 773
Vanden Berk, D. E., Richards, G. T., Bauer, A. et al. 2001, AJ, 122, 549
Worseck, G., Prochaska, J. X., McQuinn, M., et al. 2011, ApJ, 733, L24
Zheng, W., Kriss, G. A., Telfer, R. C., Grimes, J. P., & Davidsen, A. F. 1998, ApJ, 492, 855

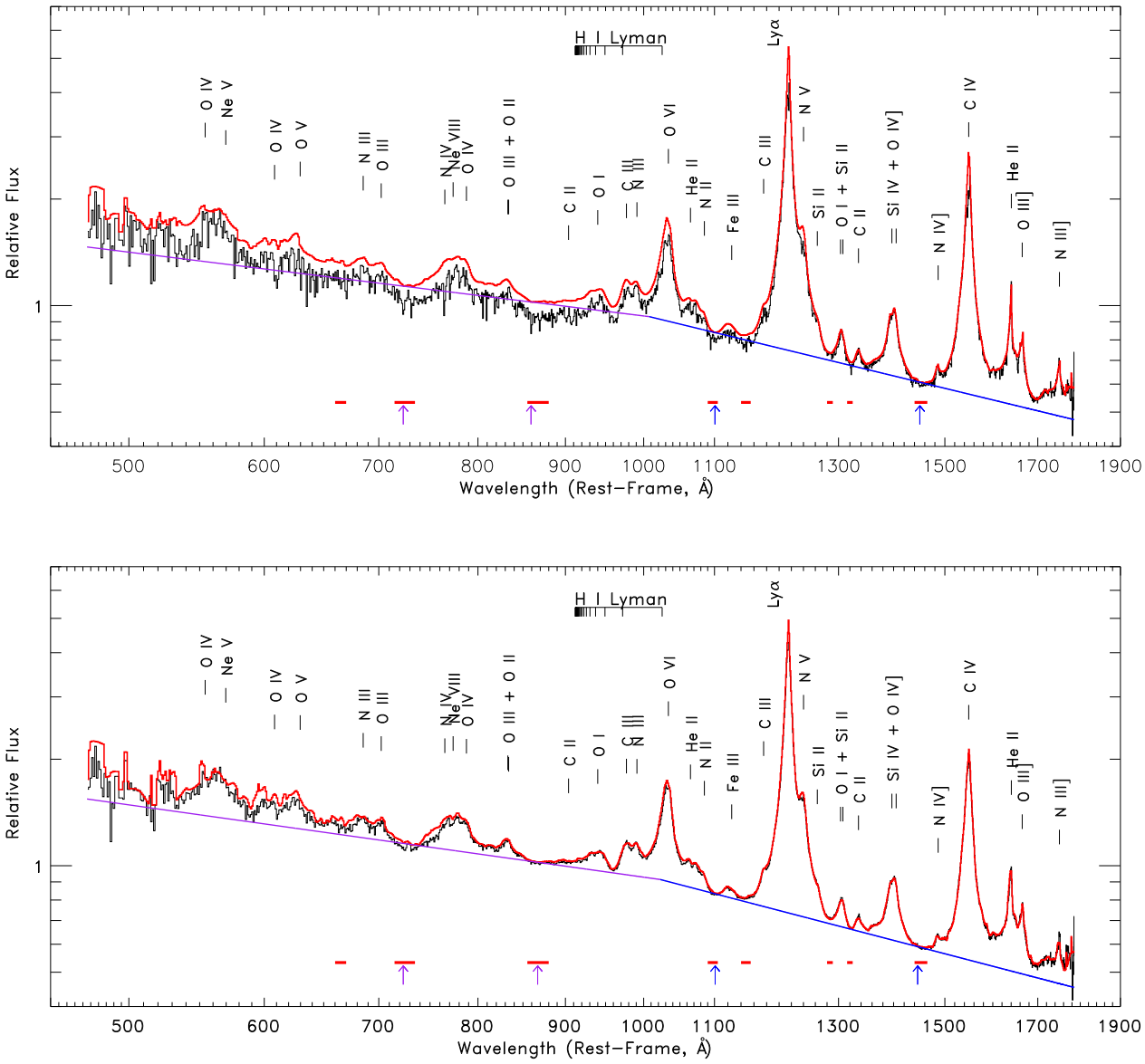

FIG. 5.— Composite spectra with rest-frame wavelengths 465–1750 Å made from 159 AGN with redshifts $0.001 \leq z_{\rm AGN} \leq 1.476$, resampled to 0.1 Å, plotted in 1 Å bins, normalized to unit flux at 1100 Å, and showing broad FUV and EUV emission lines atop a power-law continuum. Eight continuum windows are shown as small red boxes along bottom. Composite data are shown in black; red curve is composite of individual spline fits. (Top) Geometric-mean-combined *HST*/COS spectrum with frequency distribution, $F_\nu \propto \nu^{\alpha_\nu}$, with break at $\lambda_{\rm br} \approx 1000$ Å and spectral indices $\alpha_\nu = -1.41 \pm 0.15$ (EUV, $\lambda < 1000$ Å) and $\alpha_\nu = -0.83 \pm 0.09$ (FUV, $\lambda > 1200$ Å). (Bottom) Median-combined composite, with break at $\lambda_{\rm br} \approx 1025$ Å and spectral indices $\alpha_\nu = -1.32 \pm 0.15$ (EUV) and $\alpha_\nu = -0.74 \pm 0.09$ (FUV).

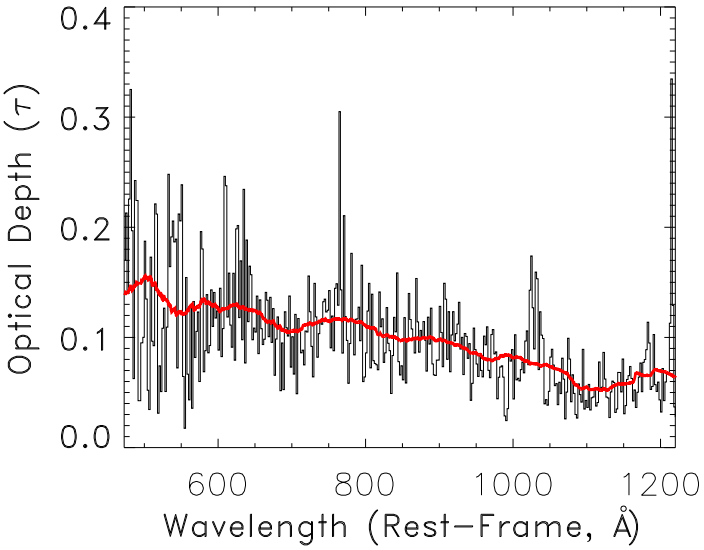

FIG. 6.— Optical depth arising from continuum line-blanketing by the Lyα forest, calculated from the difference in fluxes (top panel of Figure 5) between spline-fit continuum and line-blanketed data, and binned by 20 pixels of 0.1 Å width. Red overplot shows optical depth, smoothed over 1000 pixels.

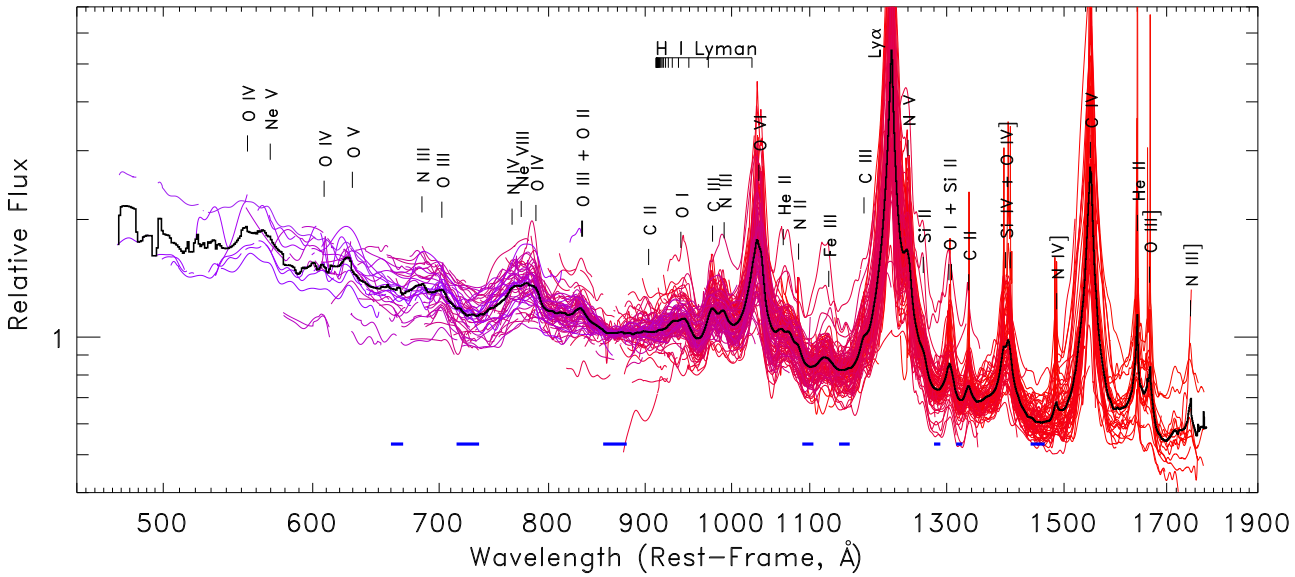

FIG. 7.— Montage of spectra of the 159 individual AGN that go into the composite spectrum (solid line), showing the range of spectral slopes and variations in emission-line strengths. The line-free continuum windows are shown as blue bars along bottom.

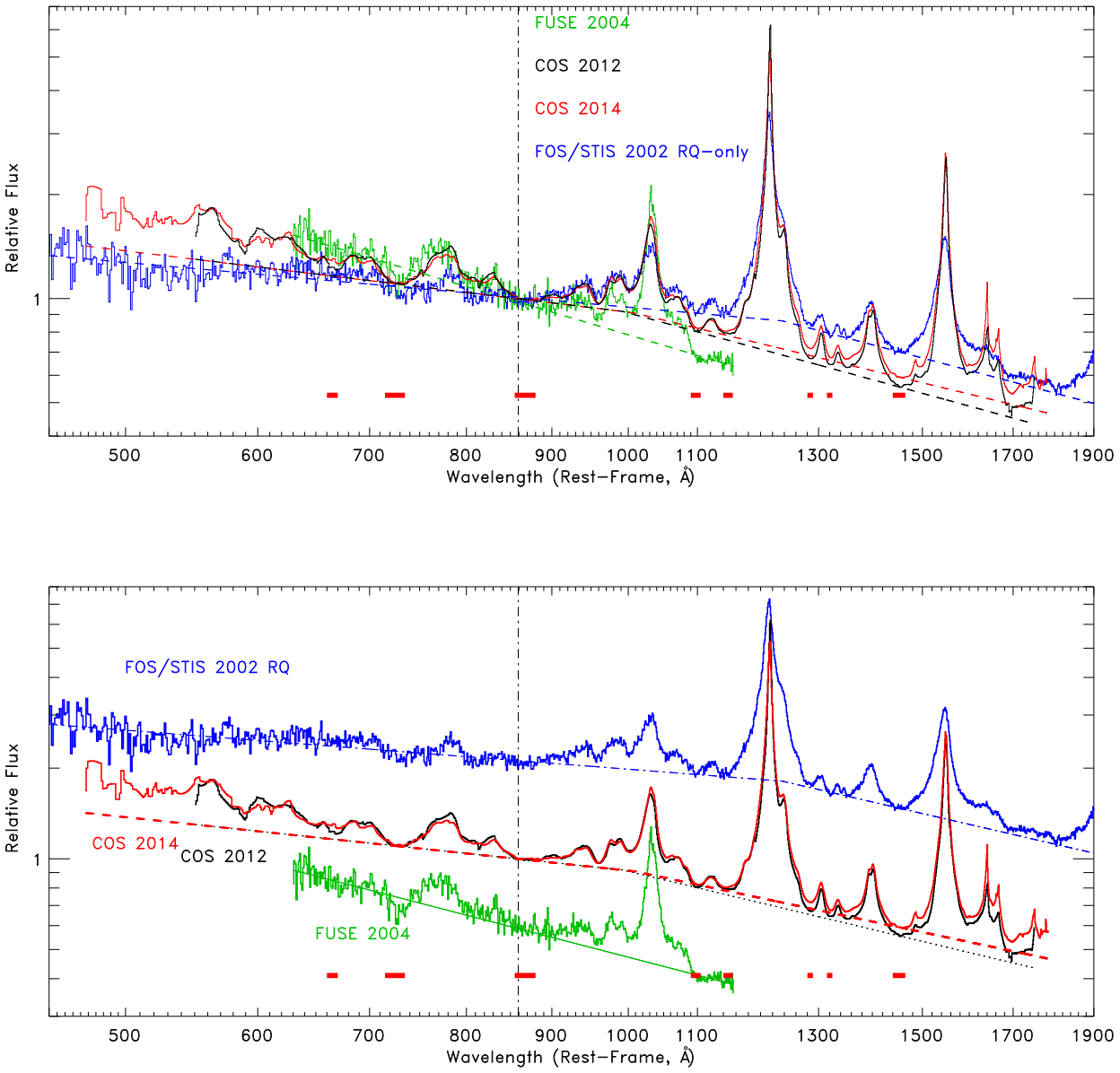

FIG. 8.— Comparison of the AGN composite spectra from FUSE (Scott et al. 2004), HST/FOS+STIS (Telfer et al. 2004), and two surveys with HST/COS (Shull et al. 2012; Stevans et al. 2014). *(Top.)* Composite spectra, F_λ, all normalized at the 860 Å line-free continuum window. Dashed lines show underlying power-law continua. The COS (2012, 2014) composite spectra, $F_\nu \propto \nu^{\alpha_\nu}$, have essentially the same EUV spectral index, $\alpha_\nu = -1.41 \pm 0.15$. FOS/STIS spectrum has $\alpha_\nu = -1.57 \pm 0.17$ for 39 radio-quiet QSOs. FUSE spectrum is harder with $\alpha_\nu = -0.56^{+0.38}_{-0.28}$ based on lower-redshift AGN. *(Bottom.)* Spectra offset vertically for clarity. The different slopes arise from fitting the continuum beneath prominent broad EUV emission lines (Ne VIII, O III, O IV, O V) and HST/COS wavelength coverage spanning an intrinsically curved AGN spectrum. Access to line-free continuum windows above and below 1100 Å (red bars along bottom) allows us to fit different FUV and EUV continuum slopes with a break at $\lambda_{\rm br} \approx 1000 \pm 25$ Å.

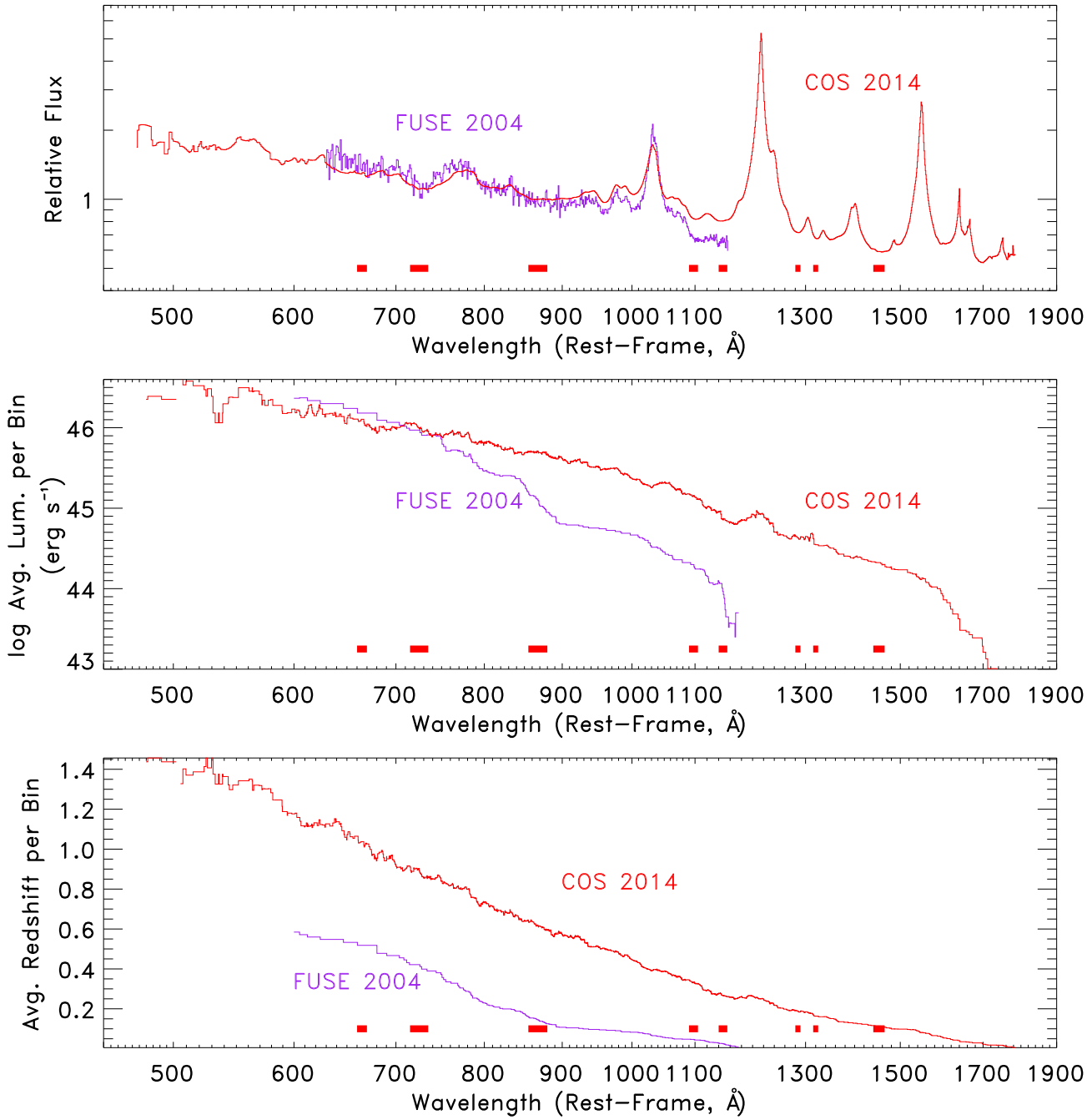

FIG. 9.— Comparison of composite spectra from COS and *FUSE*, with line-free continuum windows shown as red boxes at 660-670 Å, 720-730 Å, 855-880 Å, 1090-1105 Å, 1140-1155 Å, 1280-1290 Å, 1315-1325 Å, and 1440-1465 Å. *(Top).* Aligned composite spectra of COS and *FUSE*, normalized to 1 at 860 Å. Spectra agree at short wavelengths ($\lambda \leq 1000$ Å) but the *FUSE* fluxes show a sudden drop-off longward of 1100 Å in continuum windows at 1100 Å and 1145 Å. *(Middle).* Average AGN luminosity per wavelength bin. We plot the geometric mean luminosity, λL_λ, at 1000 Å. *(Bottom).* Average redshift of AGN per wavelength bin. The *FUSE* survey samples AGN at lower redshift than COS, with AGN luminosities comparable at $\lambda < 800$ Å, but much lower at $\lambda > 900$ Å.

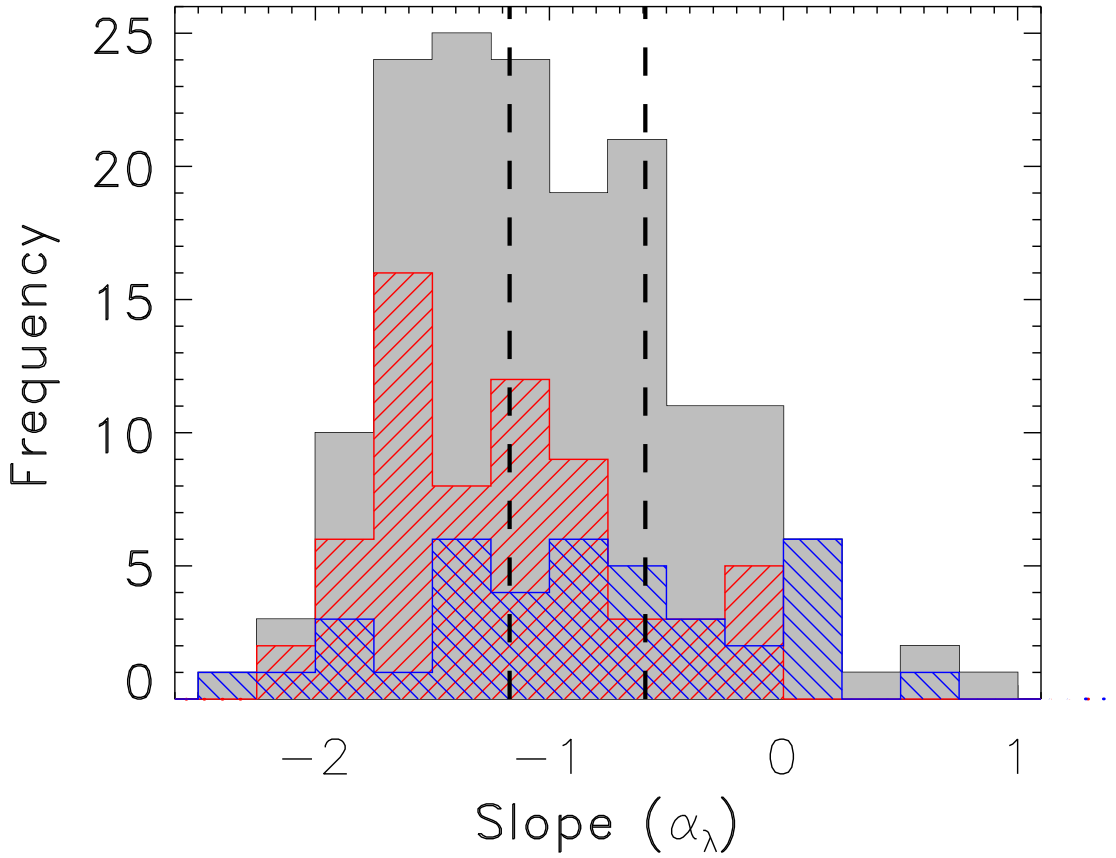

FIG. 10.— Distributions in spectral index, α_λ, vs. redshift for 159 *HST*/COS AGN, where $(\alpha_\lambda + \alpha_\nu) = -2$. Two vertical dashed lines mark mean values: $\langle\alpha_\lambda\rangle = -0.59$ for rest-frame EUV (500-1000 Å) and $\langle\alpha_\lambda\rangle = -1.17$ for rest-frame FUV (1200-2000 Å). Red histogram shows spectra using two continuum windows redward of the 1000 Å break; blue histogram shows spectra using two continuum windows blueward of the break.

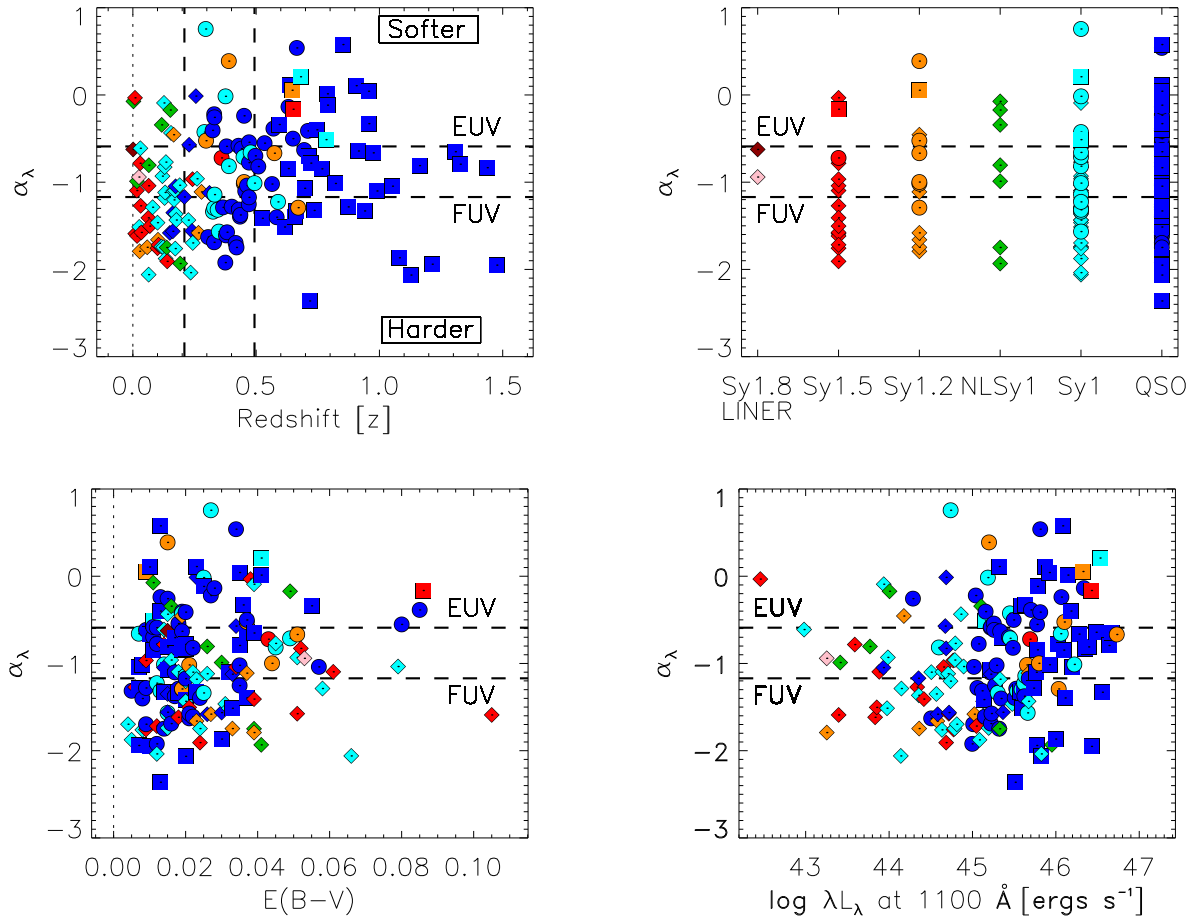

FIG. 11.— (Top Left) Spectral index, α_λ, vs. redshift for 159 *HST*/COS AGN. (Top Right) Index vs. activity type compiled by NED. (Bottom Left) Index vs. $E(B-V)$. (Bottom Right) Index vs. 1100 Å monochromatic luminosity. Two low-luminosity AGN (NGC 4395 and NGC 4051) with $\log \lambda L_\lambda \leq 41$) are omitted for clarity. Redshift and luminosity are correlated in these composites, because of curvature in the underlying spectral shape. Two horizontal lines mark mean values of this index: $\langle \alpha_\lambda \rangle = -0.59$ for rest-frame EUV (500-1000 Å); and $\langle \alpha_\lambda \rangle = -1.17$ for rest-frame FUV (1200-2000 Å). Vertical lines mark boundaries between targets designated as low-redshift ($z < 0.2$), intermediate-redshift ($0.2 < z < 0.5$), and high-redshift ($z > 0.5$). Colors denote AGN activity type: dark blue (QSO); cyan (Sy1); green (NLSy1); orange (Sy1.2); red (Sy1.5); pink (LINER); brown (Sy1.8). Symbol shapes refer to windows used to fit continua: diamonds longward of 1000 Å, squares shortward of 1000 Å, circles straddling 1000 Å with one window each in EUV and FUV.

TABLE 1
COS Observations (159 AGN Targets ordered by redshift)

AGN[a] Target	AGN[a] Type	z[a]	α_λ	F_0[a] (1100 Å)	F_λ[a] (1300 Å)	$\log(\lambda L_\lambda)$[a] (1100 Å)	$(S/N)_{res}$[a]
NGC4395	Sy 1.8	0.001064	-0.62 ± 0.006	0.188	0.16	39.70	4 , 4
NGC4051	NLSy 1	0.002336	-0.07 ± 0.002	0.809	0.83	41.02	16, 13
NGC3516	Sy 1.5	0.008836	-0.03 ± 0.007	1.54	1.1	42.46	14, 12
NGC3783	Sy 1.5	0.00973	-1.59 ± 0.1	11.0	3.6	43.40	21, 17
NGC7469	Sy 1.5	0.016317	-1.10 ± 0.03	11.9	6.4	43.88	28, 18
Mrk1044	NLSy 1	0.016451	-0.99 ± 0.007	3.98	2.6	43.41	19, 13
NGC5548	Sy 1.5	0.017175	-1.62 ± 0.003	9.56	7.0	43.83	28, 19
AKN564	LINER	0.024684	-0.94 ± 0.02	1.20	0.67	43.25	9 , 7
Mrk335	Sy 1	0.025785	-1.51 ± 0.009	5.82	4.1	43.98	24, 18
ESO031–G008	Sy 1.2	0.027619	-1.79 ± 0.01	0.958	0.62	43.25	9 , 7
Mrk290	Sy 1.5	0.029577	-0.78 ± 0.003	1.80	1.8	43.59	20, 16
Mrk279	Sy 1	0.030451	-0.61 ± 0.003	0.419	0.49	42.98	8 , 7
Mrk817	Sy 1.5	0.031455	-1.27 ± 0.0003	8.92	9.4	44.34	38, 24
Mrk509	Sy 1.5	0.034397	-1.58 ± 0.02	17.8	12.6	44.72	63, 55
PG1011-040	Sy 1.2	0.058314	-1.75 ± 0.01	2.63	2.7	44.36	26, 13
Mrk1513	Sy 1.5	0.062977	-1.41 ± 0.02	2.55	5.7	44.42	27, 15
MR2251-178	Sy 1.5	0.06398	-1.04 ± 0.009	4.26	25.3	44.65	33, 25
RXJ0503.1-6634	Sy 1	0.064	-2.06 ± 0.05	1.30	2.2	44.14	16, 8
SDSSJ145108.76+270926.9	NLSy 1	0.0645	-0.81 ± 0.008	0.539	0.92	43.77	10, 8
RBS563	Sy 1.5	0.069	-1.50 ± 0.005	0.574	9.0	43.85	13, 7
SDSSJ031027.82-004950.7	Sy 1	0.080139	-1.29 ± 0.03	0.827	1.0	44.15	10, 8
PG0804+761	Sy 1	0.101	-1.46 ± 0.007	11.0	9.6	45.48	51, 33
IRAS-F22456-5125	Sy 1.5	0.101	-1.76 ± 0.0006	2.18	2.5	44.77	44, 24
UKS-0242-724	Sy 1.2	0.1018	-1.66 ± 0.007	1.34	1.1	44.58	13, 9
IRAS-F04250-5718	Sy 1.5	0.104	-1.72 ± 0.001	3.76	3.7	45.05	63, 34
TonS210	Sy 1	0.116	-1.74 ± 0.002	4.18	3.7	45.19	36, 21
Q1230+0115	NLSy 1	0.117	-0.34 ± 0.002	3.33	4.2	45.10	51, 31
HS0033+4300	Sy 1	0.12	-0.93 ± 0.02	0.241	0.12	43.99	6 , 7
Mrk106	Sy 1	0.122951	-1.75 ± 0.004	1.44	1.1	44.79	23, 14
SDSSJ152139.66+033729.2	Sy 1	0.126354	-0.09 ± 0.01	0.192	0.17	43.94	5 , 4
Mrk876	Sy 1	0.129	-1.18 ± 0.004	4.56	3.8	45.33	56, 31
IRASL06229-6434	Sy1	0.129	-0.83 ± 0.02	1.03	0.70	44.68	16, 9
PG0838+770	Sy 1	0.131	-1.12 ± 0.005	1.05	0.83	44.71	24, 11
PG1626+554	Sy 1	0.133	-1.88 ± 0.0005	2.41	2.2	45.08	24, 14
QSO0045+3926	Sy 1	0.134	-0.77 ± 0.02	1.22	0.77	44.79	29, 20
PKS0558-504	NLSy 1	0.1372	-1.75 ± 0.02	3.94	2.8	45.33	15, 7
SDSSJ094733.21+100508.7	Sy 1.5	0.139297	-1.91 ± 0.004	0.868	0.65	44.68	11, 6
SDSSJ135712.61+170444.1	QSO	0.1505	-1.58 ± 0.005	0.584	0.44	44.58	12, 8
SDSSJ112114.22+032546.7	NLSy 1	0.152033	-0.17 ± 0.02	0.15	0.10	44.01	4 , 3
PG1115+407	Sy 1	0.154567	-0.44 ± 0.002	1.04	1.0	44.86	19, 11
SDSSJ095915.65+050355.1	QSO	0.162296	-1.56 ± 0.006	0.674	0.56	44.72	11, 7
SDSSJ135625.55+251523.7	Sy1	0.164009	-1.35 ± 0.004	0.464	0.39	44.57	8 , 5
SDSSJ015530.02-085704.0	Sy 1	0.164427	-1.10 ± 0.004	0.4	0.35	44.51	9 , 6
PG1202+281	Sy 1.2	0.1653	-0.46 ± 0.005	0.186	0.16	44.18	7 , 5
PG1048+342	Sy 1	0.167132	-1.20 ± 0.003	0.657	0.59	44.74	18, 12
SDSSJ121114.56+365739.5	Sy 1	0.170796	-1.09 ± 0.003	0.502	0.44	44.64	10, 7
SDSSJ134231.22+382903.4	Sy 1	0.171869	-1.76 ± 0.002	0.488	0.49	44.63	10, 6
1SAXJ1032.3+5051	QSO	0.173128	-1.05 ± 0.007	0.095	0.08	43.93	9 , 5
SDSSJ021218.32-073719.8	Sy 1	0.17392	-1.37 ± 0.006	0.251	0.21	44.36	8 , 5
PG1116+215	Sy 1	0.1763	-1.43 ± 0.003	5.04	4.4	45.67	34, 22
2masx-j01013113+4229356	Sy 1	0.19	-1.04 ± 0.05	0.71	0.37	44.89	8 , 6
PHL1811	NLSy 1	0.192	-1.93 ± 0.02	7.95	5.5	45.95	34, 18
SDSSJ123604.02+264135.9	QSO	0.208995	-1.17 ± 0.01	0.165	0.19	44.35	7 , 5
PG1121+422	Sy 1	0.225025	-1.43 ± 0.005	0.831	0.88	45.13	16, 10
SDSSJ001224.01-102226.5	QSO	0.228191	-0.57 ± 0.006	0.283	0.21	44.67	7 , 5
PG0953+414	Sy 1	0.2341	-2.04 ± 0.001	3.80	4.3	45.83	33, 20
SDSSJ092909.79+464424.0	QSO	0.239959	-1.56 ± 0.002	1.24	1.3	45.37	14, 9
SDSSJ133053.27+311930.5	Sy 1.5	0.242204	-0.97 ± 0.002	0.308	0.44	44.77	10, 7
RXJ0439.6-5311	Sy 1	0.243	-1.70 ± 0.002	0.337	0.36	44.81	14, 8
FBQSJ1010+3003	QSO	0.255778	-0.01 ± 0.004	0.224	0.38	44.68	15, 9
SDSSJ115758.72-002220.8	Sy 1	0.260247	-0.96 ± 0.02	0.274	0.57	44.79	8 , 5
SDSSJ134206.56+050523.8	Sy 1.2	0.266015	-1.58 ± 0.007	0.446	0.81	45.02	10, 7
PKS1302-102	Sy 1.2	0.2784	-1.11 ± 0.01	1.79	1.6	45.67	23, 16
Ton580	Sy 1	0.290237	-0.43 ± 0.002	0.974	0.97	45.45	18, 12
SDSSJ092837.98+602521.0	Sy 1	0.29545	$+0.76 \pm 0.005$	0.182	0.21	44.74	5 , 5
H1821+643	Sy 1.2	0.2968	-0.52 ± 0.007	4.16	3.4	46.10	52, 7
SDSSJ091235.42+295725.4	QSO	0.305331	-1.63 ± 0.004	0.098	0.13	44.50	6 , 5
SDSSJ082633.51+074248.3	QSO	0.310643	-1.12 ± 0.009	0.491	0.52	45.22	9 , 6
SDSSJ120720.99+262429.1	QSO	0.323529	-0.41 ± 0.003	0.387	0.40	45.16	8 , 7
SDSSJ134251.60-005345.3	Sy 1	0.325	-1.34 ± 0.005	0.535	0.62	45.30	10, 7
SDSSJ092554.43+453544.4	QSO	0.329478	-1.69 ± 0.008	0.429	0.63	45.22	13, 11
PG1001+291	Sy 1	0.3297	-1.30 ± 0.003	0.999	1.1	45.59	18, 14
PG0832+251	QSO	0.329773	-0.22 ± 0.005	0.282	0.30	45.04	12, 10
SDSSJ132704.13+443505.0	QSO	0.330709	-0.26 ± 0.004	0.0494	0.07	44.29	4 , 4

TABLE 1 — *Continued*

AGN[a] Target	AGN[a] Type	z^a	α_λ	$F_0{}^a$ (1100 Å)	$F_\lambda{}^a$ (1300 Å)	$\log(\lambda L_\lambda)^a$ (1100 Å)	$(S/N)_{res}{}^a$
PG1216+069	Sy 1	0.3313	-1.14 ± 0.02	1.10	1.2	45.63	20, 15
RXJ2154.1-4414	Sy 1	0.344	-1.32 ± 0.001	0.802	1.0	45.54	24, 16
B0117-2837	Sy 1	0.348858	-1.57 ± 0.03	1.04	1.2	45.66	21, 17
PG1049-005	Sy 1.5	0.3599	-0.72 ± 0.02	1.03	0.82	45.69	11, 10
SDSSJ094952.91+390203.9	QSO	0.365562	-1.29 ± 0.002	0.677	0.76	45.53	11, 9
SDSSJ132222.68+464535.2	QSO	0.374861	-1.92 ± 0.002	0.189	0.25	45.00	8 , 6
SDSSJ122035.10+385316.4	Sy 1	0.375767	-0.02 ± 0.01	0.29	0.28	45.18	6 , 6
SDSSJ024250.85-075914.2	QSO	0.377651	-1.61 ± 0.003	0.263	0.33	45.15	7 , 6
SDSSJ123335.07+475800.4	QSO	0.38223	-0.59 ± 0.009	0.304	0.30	45.22	9 , 8
SDSSJ134246.89+184443.6	QSO	0.382	-1.57 ± 0.004	0.308	0.40	45.23	8 , 7
SDSSJ121037.56+315706.0	Sy 1.2	0.389041	$+0.39 \pm 0.003$	0.276	0.26	45.20	7 , 8
HB89-0202-765	Sy 1	0.38939	-0.82 ± 0.01	0.0688	0.23	44.60	9 , 8
SDSSJ110312.93+414154.9	QSO	0.401023	-1.28 ± 0.009	0.186	0.21	45.06	9 , 7
SDSSJ133045.15+281321.4	QSO	0.416754	-1.70 ± 0.006	0.151	0.21	45.01	10, 7
SDSSJ111754.31+263416.6	QSO	0.420466	-1.75 ± 0.03	0.303	0.38	45.32	9 , 7
SDSSJ143511.53+360437.2	QSO	0.428593	-0.58 ± 0.3	0.231	0.24	45.22	7 , 6
HE0435-5304	QSO	0.427	-1.31 ± 0.0009	0.179	0.24	45.12	12, 7
SDSSJ110406.94+314111.4	QSO	0.434356	-1.39 ± 0.005	0.432	0.52	45.51	10, 8
B0120-28	QSO	0.436018	-1.38 ± 0.002	0.558	0.54	45.62	15, 12
SDSSJ161649.42+415416.3	QSO	0.440417	-0.62 ± 0.003	0.236	0.23	45.26	8 , 6
SDSSJ080359.23+433258.4	Sy 1	0.448706	-0.71 ± 0.02	0.351	0.13	45.45	7 , 5
TON236	Sy 1.2	0.4473	-1.02 ± 0.003	0.556	0.59	45.65	15, 12
PG0003+158	Sy 1.2	0.4509	-1.00 ± 0.05	0.769	0.70	45.80	20, 15
HE0153-4520	QSO	0.451	-0.24 ± 0.002	1.43	1.4	46.07	22, 15
SDSSJ100902.06+071343.8	QSO	0.455631	-1.10 ± 0.1	0.194	0.16	45.21	6 , 5
SDSSJ091029.75+101413.6	QSO	0.463194	-1.04 ± 4.4	0.12	0.07	45.02	4 , 5
SDSSJ082024.21+233450.4	QSO	0.470212	-1.25 ± 0.01	0.207	0.21	45.27	9 , 5
SDSSJ161916.54+334238.4	QSO	0.470946	-1.17 ± 0.9	0.523	0.40	45.67	12, 11
SDSSJ092554.70+400414.1	QSO	0.471139	-0.78 ± 0.007	0.131	0.14	45.08	6 , 4
SDSSJ123304.05-003134.1	QSO	0.471167	-0.54 ± 0.007	0.199	0.22	45.26	9 , 6
PG1259+593	Sy 1	0.4778	-0.66 ± 0.001	1.22	1.4	46.06	29, 19
HE0226-4110	Sy 1	0.493368	-1.01 ± 0.003	1.65	2.1	46.22	29, 19
SDSSJ155048.29+400144.9	QSO	0.496843	-0.70 ± 0.2	0.265	0.19	45.44	7 , 6
HS1102+3441	QSO	0.508847	-0.82 ± 0.008	0.281	0.30	45.49	15, 10
SDSSJ113327.78+032719.1	QSO	0.525073	-1.41 ± 0.3	0.117	0.12	45.14	7 , 5
SDSSJ025937.46+003736.3	QSO	0.534178	-0.55 ± 0.05	0.486	0.32	45.78	7 , 7
SDSSJ094331.61+053131.4	QSO	0.564336	-1.02 ± 0.1	0.139	0.17	45.29	6 , 4
SDSSJ040148.98-054056.5	QSO	0.570076	-0.39 ± 0.03	0.35	0.16	45.70	8 , 6
PKS0405-123	Sy 1.2	0.574	-0.67 ± 0.01	3.69	3.2	46.73	63, 29
SDSSJ124154.02+572107.3	QSO	0.583237	-1.40 ± 0.003	0.145	0.22	45.34	9 , 6
SDSSJ095000.73+483129.3	Sy 1	0.588734	-1.23 ± 0.004	0.268	0.42	45.62	8 , 5
SDSSJ225738.20+134045.4	QSO	0.593937	-0.34 ± 0.04	0.243	0.19	45.59	7 , 6
SDSSJ022614.46+001529.7	QSO	0.6151	-1.51 ± 0.01	0.229	0.34	45.60	10, 6
SDSSJ105945.23+144142.9	QSO	0.630543	-0.84 ± 0.01	0.327	0.29	45.78	10, 8
HE0238-1904	QSO	0.631	-0.14 ± 0.005	1.17	1.3	46.34	23, 18
SDSSJ111239.11+353928.2	QSO	0.635784	$+0.11 \pm 0.01$	0.112	0.11	45.32	6 , 4
3C263	Sy 1.2	0.646	$+0.05 \pm 0.02$	1.08	0.87	46.33	30, 20
SDSSJ093518.19+020415.5	QSO	0.649117	-0.50 ± 0.01	0.158	0.17	45.49	6 , 5
PKS0637-752	Sy 1.5	0.653	-0.16 ± 0.1	1.35	0.70	46.43	20, 15
SDSSJ080908.13+461925.6	QSO	0.656338	-1.39 ± 0.02	0.637	0.79	46.11	12, 10
SDSSJ105958.82+251708.8	QSO	0.661907	-1.33 ± 0.004	0.198	0.33	45.61	9 , 7
SDSSJ154553.48+093620.5	QSO	0.665	$+0.54 \pm 1.2$	0.31	-0.0	45.81	1 , 6
3C57	Sy 1.2	0.670527	-1.29 ± 0.04	0.506	0.77	46.03	21, 12
PKS0552-640	Sy 1	0.68	$+0.21 \pm 0.2$	1.53	1.0	46.53	24, 18
SDSSJ151428.64+361957.9	QSO	0.694596	-0.63 ± 0.02	0.0922	0.14	45.33	4 , 4
SDSSJ144511.28+342825.4	QSO	0.696951	-1.07 ± 0.008	0.0697	0.11	45.21	7 , 5
SDSSJ113457.62+255527.9	QSO	0.710078	-0.41 ± 0.06	0.264	0.24	45.81	8 , 7
SDSSJ155504.39+362848.0	QSO	0.713654	-0.70 ± 0.01	0.0901	0.16	45.35	7 , 4
SDSSJ124511.25+335610.1	QSO	0.717	-2.36 ± 0.8	0.129	0.23	45.51	7 , 8
SDSSJ155304.92+354828.6	QSO	0.721814	-0.78 ± 0.01	0.409	0.50	46.02	8 , 6
SDSSJ091440.38+282330.6	QSO	0.735345	-1.32 ± 0.01	0.139	0.23	45.57	8 , 6
SDSSJ100102.55+594414.3	QSO	0.746236	-0.40 ± 0.3	0.546	0.58	46.18	11, 9
SBS1108+560	QSO	0.766619	-0.85 ± 0.7	0.419	0.01	46.10	4 , 10
SDSSJ143726.14+504555.8	Sy 1	0.783319	-0.51 ± 0.1	0.0456	0.04	45.16	4 , 4
SDSSJ102218.99+013218.8	QSO	0.789304	$+0.01 \pm 0.03$	0.437	0.34	46.15	8 , 6
SDSSJ234500.43-005936.0	QSO	0.789429	-0.12 ± 0.08	0.188	0.12	45.78	7 , 5
SDSSJ101622.60+470643.3	QSO	0.821527	-1.01 ± 0.4	0.238	0.40	45.92	8 , 5
SBS1122+594	QSO	0.852	$+0.58 \pm 0.1$	0.313	0.26	46.08	12, 9
SDSSJ141910.20+420746.9	QSO	0.873501	-1.28 ± 0.07	0.132	0.21	45.73	7 , 4
SDSSJ112244.89+575543.0	QSO	0.905906	$+0.11 \pm 0.005$	0.166	0.20	45.87	7 , 5
FBQSJ0751+2919	QSO	0.915	-0.64 ± 0.02	0.66	0.68	46.48	26, 19
PG1407+265	QSO	0.946	-1.33 ± 0.06	0.733	1.1	46.56	33, 20
HB89-0107-025-NED05	QSO	0.956	$+0.04 \pm 0.07$	0.162	0.12	45.92	12, 8
LBQS-0107-0235	QSO	0.957039	-0.33 ± 0.08	0.0834	0.07	45.63	11, 10
PG1148+549	QSO	0.975	-0.66 ± 0.01	0.351	0.46	46.28	25, 15

TABLE 1 — *Continued*

AGN[a] Target	AGN[a] Type	z[a]	α_λ	F_0[a] (1100 Å)	F_λ[a] (1300 Å)	$\log(\lambda L_\lambda)$[a] (1100 Å)	$(S/N)_{res}$[a]
SDSSJ084349.49+411741.6	QSO	0.989986	-1.10 ± 0.2	0.104	0.08	45.77	5 , 5
HE0439-5254	QSO	1.053	-1.05 ± 0.04	0.241	0.38	46.20	14, 9
SDSS-J100535.24+013445.7	QSO	1.0809	-1.87 ± 0.09	0.143	0.27	46.00	11, 11
FIRST-J020930.7-043826	QSO	1.131	-2.06 ± 0.02	0.0858	0.25	45.82	13, 13
PG1206+459	QSO	1.16254	-0.81 ± 1.1	0.296	0.40	46.39	21, 16
PG1338+416	QSO	1.21422	-1.94 ± 0.4	0.0632	0.18	45.77	16, 11
LBQS-1435-0134	QSO	1.30791	-0.65 ± 0.01	0.418	0.59	46.67	26, 20
PG1522+101	QSO	1.32785	-0.79 ± 0.3	0.372	0.43	46.64	19, 14
Q0232-042	QSO	1.43737	-0.83 ± 0.3	0.158	0.22	46.35	15, 12
PG1630+377	QSO	1.47607	-1.95 ± 0.1	0.176	0.70	46.43	25, 10

[a] Our 159 AGN targets, types, redshifts, fluxes, spectral indices, luminosities, and S/N ratios. All fluxes in units of 10^{-14} erg cm^{-2} s^{-1} Å^{-1}. Rest-frame, dereddened spectral distributions are fitted to power laws, $F_\lambda = F_0(\lambda/1100\ \text{Å})^{\alpha_\lambda}$. Wavelength index α_λ corresponds to frequency index $\alpha_\nu = -[2 + \alpha_\lambda]$. The eight columns show: (1) AGN target; (2) AGN type; (3) AGN redshift; (4) Fitted spectral index, α_λ, with statistical errors; (5) Rest-frame flux normalization F_0 at 1100 Å; (6) Observed flux F_λ at 1300 Å; (7) Band luminosity, λL_λ at 1100 Å (in erg s^{-1}); (8) signal-to-noise at 1250 Å and 1550 Å for data with G130M (1132–1460 Å) and G160M (1394–1798 Å) gratings, respectively. Flux at 1300 Å for SBS 1108+560 (noted with *) is low, owing to LyC absorption ($\lambda < 1334$ Å) from a LLS at $z = 0.46335$. Finn et al. (2014) fitted a harder spectral index, $\alpha_\lambda = -0.64$, for J0209-0438 at $z = 1.131$, using additional COS/G230L spectra extending to longer wavelengths.

TABLE 2
LYMAN-LIMIT SYSTEMS AND PARTIAL LYMAN-LIMIT SYSTEMS

AGN Target	$z_{\rm LLS}$[a] (redshift)	log $N_{\rm HI}$[a] ($N_{\rm HI}$ in cm^{-2})	b[a] (km s^{-1})
SDSSJ115758.72-002220.8	0.25661	15.25 ± 0.03	25
SDSSJ092554.43+453544.4	0.25057	15.14 ± 0.03	25
	0.30959	15.27 ± 0.03	25
PG1216+069	0.28231	16.29 ± 0.01	34
B0117-2837	0.34833	15.52 ± 0.05	25
	0.34866	16.02 ± 0.02	25
SDSSJ122035.10+385316.4	0.27332	15.61 ± 0.02	25
SDSSJ123335.07+475800.4	0.28495	15.41 ± 0.03	25
HB89-0202-765	0.30657	14.95 ± 0.03	25
SDSSJ110312.93+414154.9	0.27116	15.11 ± 0.03	25
SDSSJ133045.15+281321.4	0.27553	15.20 ± 0.02	25
SDSSJ111754.31+263416.6	0.35193	16.14 ± 0.02	25
SDSSJ143511.53+360437.2	0.26246	15.24 ± 0.02	25
	0.37292	16.72 ± 0.06	25
	0.3876	16.15 ± 0.02	25
PG0003+158	0.30573	15.47 ± 0.01	25
	0.31215	14.38 ± 0.02	25
	0.34787	15.98 ± 0.04	17
	0.36619	15.10 ± 0.02	25
	0.37034	14.68 ± 0.06	25
	0.38612	14.84 ± 0.01	25
	0.40137	15.04 ± 0.02	25
	0.42184	14.77 ± 0.02	25
HE0153-4520	0.40051	14.52 ± 0.02	25
SDSSJ100902.06+071343.8	0.35586	17.41 ± 0.04	25
	0.3745	14.28 ± 0.06	25
	0.37554	15.62 ± 0.04	25
	0.37624	14.86 ± 0.06	25
	0.41401	15.15 ± 0.02	25
SDSSJ091029.75+101413.6	0.2634	16.86 ± 0.5	25
	0.26375	14.17 ± 0.1	25
	0.26432	14.96 ± 0.03	25
	0.41924	17.14 ± 0.8	29
SDSSJ082024.21+233450.4	0.45424	14.56 ± 0.02	25
SDSSJ161916.54+334238.4	0.2694	16.40 ± 0.03	25
	0.26988	14.72 ± 0.08	25
	0.27086	14.85 ± 0.02	25
	0.2716	14.58 ± 0.08	25
	0.42676	14.93 ± 0.07	25
	0.44231	15.81 ± 0.02	25
	0.47091	16.84 ± 0.1	25
	0.47179	14.47 ± 0.03	25
SDSSJ092554.70+400414.1	0.2477	19.26 ± 0.06	59
	0.25283	14.84 ± 0.05	25
SDSSJ123304.05-003134.1	0.31875	15.51 ± 0.01	25
	0.43061	14.89 ± 0.02	25
PG1259+593	0.2924	14.49 ± 0.02	25
HE0226-4110	0.24525	14.24 ± 0.03	25
	0.49252	14.64 ± 0.05	25
SDSSJ155048.29+400144.9	0.31257	16.62 ± 0.06	41
	0.42739	15.64 ± 0.02	25
	0.4919	16.57 ± 0.02	25
	0.49255	15.69 ± 0.05	25
HS1102+3441	0.26164	14.95 ± 0.03	25
	0.28916	14.49 ± 0.04	25
	0.28986	14.89 ± 0.03	25
	0.31039	15.07 ± 0.01	25
	0.33246	14.37 ± 0.02	25
	0.50607	15.07 ± 0.02	25
SDSSJ113327.78+032719.1	0.24663	17.53 ± 0.1	25
	0.30216	14.44 ± 0.04	25
	0.45225	15.22 ± 0.03	25
SDSSJ094331.61+053131.4	0.35464	16.12 ± 0.09	91
SDSSJ040148.98-054056.5	0.32381	15.37 ± 0.01	25
	0.36547	14.60 ± 0.05	25
PKS0405-123	0.36077	15.04 ± 0.02	25
	0.4057	14.83 ± 0.02	25
SDSSJ095000.73+483129.3	0.48502	15.07 ± 0.03	25
SDSSJ225738.20+134045.4	0.37712	15.07 ± 0.02	25
	0.3787	14.90 ± 0.08	25
	0.49905	15.72 ± 0.02	25
SDSSJ022614.46+001529.7	0.4161	14.77 ± 0.02	25
SDSSJ105945.23+144142.9	0.34074	15.33 ± 0.02	25
	0.46567	15.65 ± 0.03	25
	0.57638	15.51 ± 0.03	25

TABLE 2 — *Continued*

AGN Target	$z_{\rm LLS}$[a] (redshift)	log $N_{\rm HI}$[a] ($N_{\rm HI}$ in cm^{-2})	b[a] (km s^{-1})
	0.61727	14.71 ± 0.02	25
HE0238-1904	0.3441	14.69 ± 0.02	25
	0.35534	14.87 ± 0.03	25
	0.40102	14.91 ± 0.02	25
	0.42424	15.03 ± 0.02	25
SDSSJ111239.11+353928.2	0.24679	15.45 ± 0.03	25
3C263	0.32545	15.44 ± 0.02	25
	0.52796	15.55 ± 0.01	25
SDSSJ093518.19+020415.5	0.35457	15.26 ± 0.03	25
	0.42852	14.69 ± 0.03	25
PKS0637-752	0.24326	15.86 ± 0.09	38
	0.41755	15.42 ± 0.01	25
	0.4528	15.47 ± 0.02	25
	0.46847	16.08 ± 0.03	25
SDSSJ080908.13+461925.6	0.61917	16.15 ± 0.01	25
SDSSJ154553.48+093620.5	0.47379	17.25 ± 0.2	25
	0.47623	15.62 ± 0.02	25
3C57	0.24988	15.67 ± 0.009	25
	0.29224	14.84 ± 0.02	25
	0.32332	16.29 ± 0.01	76
	0.32827	15.53 ± 0.02	25
	0.38329	14.75 ± 0.02	25
	0.5332	14.22 ± 0.08	25
PKS0552-640	0.34517	16.71 ± 0.03	25
	0.34592	14.18 ± 0.04	25
	0.446	15.89 ± 0.04	30
	0.63017	14.78 ± 0.06	25
SDSSJ151428.64+361957.9	0.41065	17.93 ± 0.2	42
SDSSJ144511.28+342825.4	0.60722	15.51 ± 0.02	25
SDSSJ113457.62+255527.9	0.2469	14.66 ± 0.03	25
	0.43233	16.40 ± 0.03	53
	0.50265	15.19 ± 0.02	25
	0.66824	15.01 ± 0.05	25
SDSSJ155504.39+362848.0	0.30689	14.57 ± 0.02	25
	0.36504	14.94 ± 0.02	25
	0.57611	15.52 ± 0.03	25
	0.60275	15.36 ± 0.02	25
SDSSJ124511.25+335610.1	0.31802	14.80 ± 0.03	25
	0.44947	15.44 ± 0.1	25
	0.55682	16.50 ± 0.2	25
	0.58762	15.14 ± 0.03	25
	0.63215	15.92 ± 0.06	65
	0.64496	15.70 ± 0.04	25
	0.64862	15.17 ± 0.04	25
	0.68918	16.68 ± 0.2	25
	0.71297	16.32 ± 0.1	35
SDSSJ155304.92+354828.6	0.4756	15.43 ± 0.03	25
	0.52027	15.18 ± 0.03	25
SDSSJ091440.38+282330.6	0.24426	15.39 ± 0.01	25
	0.59969	15.33 ± 0.02	25
SDSSJ100102.55+594414.3	0.30355	17.27 ± 0.04	25
	0.4159	16.61 ± 0.02	25
SBS1108+560	0.28646	15.91 ± 0.2	50
	0.46334	17.06 ± 0.1	35
	0.61765	15.07 ± 0.03	25
	0.68267	15.36 ± 0.02	25
SDSSJ143726.14+504555.8	0.25065	15.77 ± 0.06	25
	0.56945	15.23 ± 0.03	25
	0.76901	15.52 ± 0.08	25
	0.77109	14.94 ± 0.1	25
	0.77248	16.07 ± 0.1	36
SDSSJ102218.99+013218.8	0.39907	13.41 ± 0.09	25
	0.7425	15.35 ± 0.1	25
SDSSJ234500.43-005936.0	0.2539	16.08 ± 0.03	25
	0.54818	15.96 ± 0.07	34
SDSSJ101622.60+470643.3	0.4321	15.59 ± 0.02	25
	0.66475	15.92 ± 0.1	25
	0.72766	16.26 ± 0.3	14
	0.74627	15.43 ± 0.05	25
SBS1122+594	0.31236	14.95 ± 0.02	25
	0.31784	14.43 ± 0.04	25
	0.35115	15.14 ± 0.02	25
	0.3919	15.18 ± 0.06	25
	0.55744	15.82 ± 0.03	25
	0.55817	16.42 ± 0.02	25
	0.5698	14.72 ± 0.04	25

TABLE 2 — *Continued*

AGN Target	$z_{\rm LLS}$[a] (redshift)	log $N_{\rm HI}$[a] ($N_{\rm HI}$ in cm^{-2})	b[a] (km s^{-1})
	0.67835	15.97 ± 0.08	19
SDSSJ141910.20+420746.9	0.289	16.17 ± 0.03	25
	0.42561	16.02 ± 0.02	25
	0.52221	15.87 ± 0.02	25
	0.53461	16.06 ± 0.07	25
	0.60842	15.72 ± 0.02	25
	0.80463	15.95 ± 0.04	25
	0.84523	16.20 ± 0.03	25
SDSSJ112244.89+575543.0	0.39798	14.78 ± 0.03	25
FBQSJ0751+2919	0.43187	15.69 ± 0.01	25
	0.49455	15.56 ± 0.02	25
	0.82902	15.99 ± 0.02	25
PG1407+265	0.29717	15.13 ± 0.03	25
	0.32569	15.20 ± 0.01	25
	0.57488	15.56 ± 0.01	25
	0.59964	15.78 ± 0.03	26
	0.68278	16.39 ± 0.03	33
	0.81699	15.62 ± 0.02	25
HB89-0107-025-NED05	0.39909	16.59 ± 0.02	30
	0.53546	15.08 ± 0.03	25
	0.7178	15.37 ± 0.01	25
	0.8093	15.17 ± 0.05	25
	0.87569	15.51 ± 0.06	25
LBQS-0107-0235	0.53635	15.81 ± 0.05	86
	0.71892	15.54 ± 0.02	25
	0.87636	15.77 ± 0.02	25
PG1148+549	0.25242	15.26 ± 0.02	25
	0.57785	15.24 ± 0.01	25
	0.68864	15.52 ± 0.03	25
	0.90485	15.34 ± 0.05	25
SDSSJ084349.49+411741.6	0.53258	16.67 ± 0.05	25
	0.53346	16.10 ± 0.03	25
	0.54106	15.30 ± 0.02	25
	0.54353	15.57 ± 0.04	25
HE0439-5254	0.328	15.67 ± 0.01	25
	0.61508	16.25 ± 0.04	52
	0.86515	15.58 ± 0.03	25
SDSS-J100535.24+013445.7	0.41753	15.04 ± 0.05	25
	0.41853	16.37 ± 0.03	25
	0.41963	15.83 ± 0.02	25
	0.83711	16.81 ± 0.01	25
	0.83938	16.10 ± 0.04	25
FIRST-J020930.7-043826	0.39035	18.00 ± 0.2	49
	0.8268	15.05 ± 0.04	25
PG1206+459	0.40852	15.71 ± 0.02	25
	0.41412	15.69 ± 0.04	25
	0.92772	17.03 ± 0.08	46
PG1338+416	0.34886	16.37 ± 0.06	41
	0.46369	15.28 ± 0.01	25
	0.62136	16.30 ± 0.05	58
	0.68617	16.49 ± 0.04	32
LBQS-1435-0134	0.26228	14.96 ± 0.02	25
	0.29907	15.30 ± 0.02	25
	0.39214	15.03 ± 0.02	25
	0.43834	14.76 ± 0.02	25
	0.61283	15.30 ± 0.02	25
	0.68124	15.54 ± 0.02	25
PG-1522+101	0.51841	16.32 ± 0.2	16
	0.57179	15.31 ± 0.06	17
	0.67518	15.87 ± 0.01	25
	0.72879	16.60 ± 0.09	26
Q0232-042	0.32239	16.14 ± 0.03	30
	0.73888	16.64 ± 0.08	35
	0.80773	15.60 ± 0.05	32
PG1630+377	0.27395	16.92 ± 0.04	44
	0.27821	14.72 ± 0.02	25
	0.41774	15.72 ± 0.02	25
	0.41856	14.67 ± 0.04	25
	0.8111	15.52 ± 0.03	25
	0.91449	15.81 ± 0.01	25

[a] In these 71 AGN sight lines we find 7 Lyman Limit systems ($\log N_{\rm HI} \geq 17.2$) and 214 partial Limit limit absorbers ($15.0 \leq \log N_{\rm HI} < 17.2$). We list their redshifts, H I column densities and lower-limit statistical uncertainties, and doppler parameters (b) derived by fitting Lyα and higher Lyman series absorbers. When the doppler parameter is unconstrained, we used mean $b = 25$ km s^{-1} to propagate uncertainties in the continuum slope of individual spectra.